UNIVERSITY OF KWAZULU-NATAL

Using JVLA to remove CMB foregrounds

by

Onkabetse Sengate

Submitted in fulfilment of the
academic requirements for the degree of
Master of Science,
in the
School of Chemistry and Physics,
University of KwaZulu-Natal

Durban
September 2016

Signed:  Name: Prof. Jonathan Sievers 15 February 2017

A person who never made mistake never tried anything new. - Albert Einstein

Abstract

The Cosmic Microwave Background (CMB) is the radiation that fills the universe left over from the Big Bang. The CMB is an important tool in cosmology as it holds within it the structure of the early universe. It is from CMB observations that we have learned most of what we know about the large-scale properties of the universe, such as its age, what it is made of, and its future fate. The CMB can also be used to measure things like the total relativistic energy in the universe, the mass of the neutrino, the matter fluctuation power spectrum, and the thermal energy content and peculiar velocities of clusters of galaxies. Precise measurement of this radiation remains the main goal of many cosmological studies. However, cosmologists face limitations when observing CMB due to instrumental systematics and foregrounds. The foreground radiation comes from gas and dust within the milky way, dusty star-forming galaxies (DSFGs), radio galaxies and active galactic nuclei, amongst others. On small scales, DSFGs are the most challenging foreground because they are clustered, and hence their power spectrum does not scale simply like ℓ^2. These dusty galaxies currently play a major role in limiting what can be inferred from measurements by the Atacama Cosmology Telescope (ACT) and the South Pole Telescope (SPT). The situation is helped somewhat by recently released data from the Planck Satellite, but it has a factor of 3.5 times worse resolution than ACT and SPT,

and so the DSFGs remain a major foreground.

We present the power spectrum of cross-correlation between ACT and Jansky Very Large Array (JVLA). The well known radio-far Infrared correlation (R-FIR) means that the low frequency JVLA data could be used to remove the dusty star-forming galaxies very efficiently Intema et al. (2009) from high resolution CMB observations.

The ACT-JVLA cross-correlation is stronger at 220 GHz than 150 GHz as expected from dusty galaxies but not from radio point sources. Further more the correlation is stronger in small scales than large scales as expected from clustered dusty galaxies. Therefore the correlation is consistent with the clustered dusty galaxies signal. The level of the correlation is consistent with a low redshift ($z< 0.5$) origin of clustered galaxies. We finally see no evidence of the Poissoin term in cross-correlation, consistent with high redshift origin of non-clustered dusty galaxies.

Preface and Declaration

The work described in this dissertation was carried out in the School of Chemistry and Physics, University of KwaZulu-Natal, Durban, from May 2014 to September 2016, under the supervision of Prof. Jonathan Sievers.

These studies represent original work by the author and have not otherwise been submitted in any form for any degree or diploma to any tertiary institution. Where use has been made of the work of others it is duly acknowledged in the text.

Onkabetse Sengate

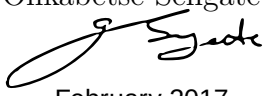

February 2017

Acknowledgments

Firstly, I want to thank the SKA South Africa for their financial support during my studies.

I also want to thank my advisor, Prof. Jonathan Sievers for his guidance and for providing all the resources I needed throughout my research.

I am also giving my thanks to my co-advisor, Dr Steven T. Myers for his assistance in data processing.

I would like to thank my colleague, Dr Kenda Knowles, who assisted during data calibration process.

Finally, I would like to thank my family for their support since I was born till now, I am who I am because of their love.

Contents

List of Tables

List of Figures

CHAPTER 1

Introduction

In trying to explain how our universe was created and what it will become ages from now, scientists and philosophers came up with different interesting theories. The currently accepted scientific theory is the "hot Big Bang theory", which tells us that the universe started from an explosion (the "Big Bang") of an intensely hot singularity about 13.7 billion years ago. This tiny ball suddenly started expanding to form the universe we see today.

According to the Big Bang model the early universe was just hot soup of plasma too hot for atoms to form. Thomson scattering held photons in place, making the universe opaque. As the universe continued expanding and cooling, at some point it was cool enough to allow electrons and protons to combine to form atoms, this epoch is known as the "Recombination Era". Recombination occurred 380 000 years after the big bang. After the formation of first atoms, the universe became transparent, allowing photons to freely travel. These photons can still be observed today and are known as the Cosmic Microwave Background (CMB). The CMB is the farthest radiation that astronomers can measure today. Astronomers refer to it as the "baby picture" of the universe, making it one of the most powerful tools to study the early universe.

The first detection of the CMB happened accidentally in 1965 when enginners Penzias and Wilson enginners while using Holmdel antenna to measure radio signals(Penzias & Wilson, 1965). The discovery of the CMB made the big bang model preferred over other theories of the origin of the universe as it proved the predictions made by Ralph Alpher (Alpher, 2014) and now fits the observed facts better than any other theory that's been proposed. Ever since this important discovery, the CMB has been observed and studied by different experiments at different frequencies and resolutions. The first measurements of fluctuations were carried out with NASA's Cosmic Background Explorer (COBE) satellite launched 1989. COBE mapped the full sky CMB temperature anisotropies on angular scales $> 7^\circ$ (Smoot et al., 1992). These measurements confirmed that the CMB has a nearly perfect blackbody spectrum with the peak temperature of 2.728 K (Fixsen et al., 1996), and is isotropic with small temperature fluctuations of one part in 10^5 (Smoot et al., 1992).

COBE observations were then followed by many other space-based and ground-based experiments which kept improving CMB maps' sensitivity and resolution. Among them, is NASA's Wilkinson Microwave Anisotropy Probe (WMAP) satellite, which started its operation in 2003. WMAP measured the CMB at a resolution of 0.2° ($\ell \sim 1200$) over 9 years (Bennett et al., 2013). The other space instrument known for intensive studies of the CMB is the European Space Agency's (ESA) Planck satellite (Planck Collaboration et al., 2015). Planck can observe up to a resolution of $5'$ ($\ell \sim 2500$) extending WMAP measurements.

The above-mentioned experiments, not forgetting many others, have now contributed a lot to the study of the universe with the CMB. They precisely studied CMB temperature anisotropies on scales of several arcminutes ($\ell < 2000$), and managed to measure with unprecedented accuracy the age, density, and compositions of the universe, to percent level accuracy, and tested the Lambda Cold Dark Matter (ΛCDM) model or "standard model" of cosmology (Hinshaw et al., 2013; Planck Collaboration et al., 2015).

Now that the CMB is well studied on large scales, most current and upcoming experiments are aimed at extending the CMB observations to arcminute scales ($\ell > 2000$) of the

CMB Silk damping tail ($500 < \ell < 3000$) (Hu & White, 1997). The South Pole Telescope (SPT) and the Atacama Cosmology Telescope (ACT) (Swetz et al., 2011) are among the instruments which have already provided high resolution CMB maps with $1.5'$ angular resolution and measured CMB power beyond the Silk damping tail. By precisely measuring CMB power spectrum at arcminutes angular scales, it can be used to measure things like the total relativistic energy in the universe (even from the possibly-as-yet-undiscovered particles), the mass of the neutrino, the matter fluctuation power spectrum, and the thermal energy content and peculiar velocities of clusters of galaxies (Sievers et al., 2013). Currently, the best limits on the absolute mass of the neutrino come not from particle physics (which measured the mass difference between the species) but cosmology (Abazajian et al., 2015).

However, the accurate measurement of the CMB is restricted by "foregrounds". As already mentioned, CMB photons are born at a much early epoch. To reach the Earth's surface, they pass through plenty of both astronomical and non-astronomical process, which some also emit microwave signals, and can obstruct the CMB photon's path or change the observed intensity.

The level at which CMB contaminated depends on the frequency and angular resolution of the observations. The large scale ($\ell < 1000$) CMB measurements are contaminated more by diffuse emissions from our own galaxy; galactic synchrotron radiation, free-free emission, and thermal emission from galactic dust. At the current state, diffuse emissions are well studied (Smoot et al., 1992; Gold et al., 2009; Planck Collaboration et al., 2015) and some templates are now available for separating them from CMB measurements (Brandt et al., 1994; Tegmark et al., 2003; Tegmark & Efstathiou, 1996; Tegmark & de Oliveira-Costa, 1997,1998), therefore temperature CMB total intensity angular spectrum is well determined at lower resolutions (Bennett et al., 2013).

On small scales of few arcminutes ($\ell > 3000$) and millimetre wavelengths, CMB anisotropies are dominated by signals from radio and infrared point sources (Dunkley et al., 2013; Keisler et al., 2011; Planck Collaboration et al., 2015; Toffolatti et al., 1999), and secondary anisotropies from Sunyaev-Zeldovich (SZ) effects (Sunyaev & Zeldovich, 1970). These pop-

ulation of sources limit what can be attained from CMB measurements from experiments such as ACT and SPT at arcminute scales. Sources bright enough to be detected are masked from the maps; fainter sources must be removed statistically. The separation of point source power from the CMB is more challenging compared to the diffuse foregrounds because of the limited knowledge of their nature.

Most radio point sources expected at mm wavelengths are synchrotron-emitting active galactic nuclei (AGNs) with flat spectrum or decreasing with wavelength (Marriage et al., 2011; Toffolatti et al., 1999; Vieira et al., 2010). Radio sources can be easily removed from CMB maps by masking as they are Poisson distributed at frequencies higher than 150 GHz (observing frequencies of ACT and SPT) and their clustering power is observed to be negligible (González-Nuevo et al., 2005; Toffolatti et al., 1998).

The infrared sources are mainly dusty star forming galaxies (DSFGs) residing at higher redshifts. These sources pose a serious problem to mm-wave CMB surveys for multiple reasons. Firstly they are confusion limited, the current CMB experiments are limited to observe up to an angular resolution of typically few arcminutes, while distant galaxies have a typical angular size of few arcseconds in the microwave sky, therefore most of them remain undetected and their emission is contained in the CMB maps. Since the DSFGs are buried in dust, they are difficult to observe at different wavelengths, so relatively little information is known about them. The situation is made worse by their clustering nature, and their clustering power contributes significantly to CMB contamination unlike radio sources (Toffolatti et al., 1999; Hall et al., 2010). Their clustering power turned to be hard to model as it does not scale simply like ℓ^2. After masking resolved bright DSFGs, the noise from faint high-z ones and the clustering power remain dominates the CMB power at $\ell \sim 3000$, therefore the CMB contamination due to high-z DSFGs remains a major problem for mm-wave CMB experiments.

The above reasons motivate the current study. We desire alternative ways of separating the residual power of DSFGs signal from CMB power. This study implements a potentially cheap method of tracing clustered DSFGs signal on the CMB maps. Our method relies on the well known Radio Far-Infrared (R-FIR) correlation that exists between radio continuum

(RC) and far-Infrared emission of galaxies(Condon, 1992). This correlation is followed by star-forming galaxies, so the R-FIR means that high sensitivity ($\sim \mu Jy$), low resolution low-frequency continuum radio data may be able to trace the most problematic DSFG signal from CMB measurements at small-scales very cheaply. Radio source counts at 1.4 GHz are dominated by AGN's above 1 mJy and DSFGs below this flux, after removal of sources brighter than 1 mJy, majority of AGN's will be removed, but few of the DSFG's.

Our study uses CMB maps from the ACT telescope as tracers of DSFGs. ACT is a currently running CMB experiment measuring CMB power spectrum up to $\ell = 10000$ (Das et al., 2014; Dunkley et al., 2011; Sievers et al., 2013). They successfully removed most foreground power from their CMB maps, but the residual DSFG signal remains the limiting factor for what can be inferred from their measurements. SPT is in a similar situation. The radio observations we used were obtained by the Jansky Very Large Array (JVLA). The JVLA at 1.4 GHz can directly measure ACT angular scales, the ones where the clustering becomes important. By reaching the confusion limit and not resolve sources, we can measure the signal of the DSFGs. The data we use is taken in the super-drift scan/On-The-Fly (OTF) mode, were antennas are allowed to continuously scan across in the Right Ascension (RA). At L-band centre of 1.5 GHz, during drift-scanning, one $30\prime$ primary beam is crossed in 2 min giving a rms sensitivity of 44 μJy/beam which is enough for detection of DSFGs. Furthermore, we assess if the JVLA data taken in a super drift scan can serve as a template for large-area surveys carried out by other radio telescopes.

1.1 CMB Foregrounds

Even though we are primarily interested in DSFG emission, this section briefly discusses different components of CMB foregrounds. Figure 1.1 shows the total intensity of extra-galactic background light (EBL) measured on the sky as a function of frequency. The CMB dominates the EBL power on the microwave domain between 10 GHz to 600 GHz but overlaps with the Radio Background (RB) at lower frequencies, and the Cosmic Infrared Background (CIB) at higher frequencies. Therefore, one can easily tell that RB and

CIB are the main extragalactic emissions contaminating the CMB.

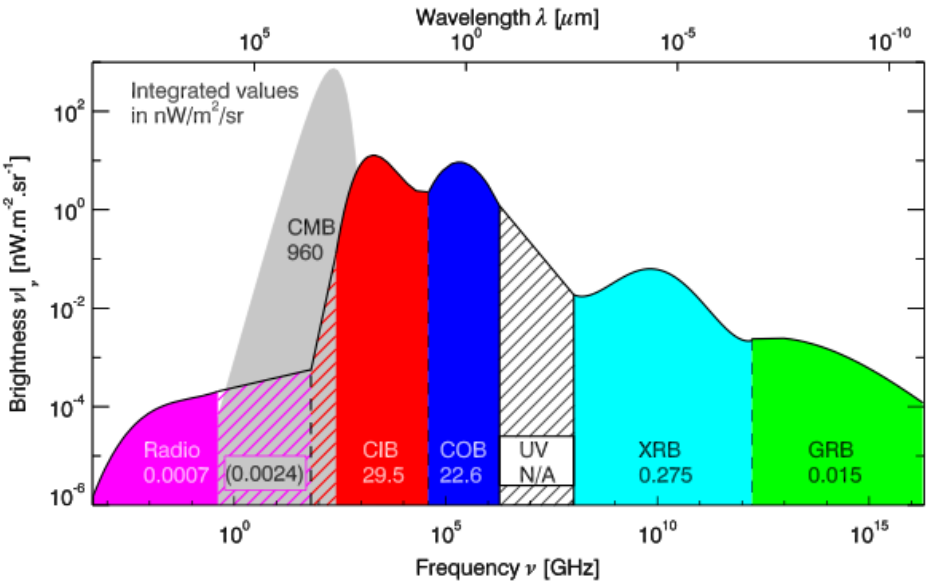

Figure 1.1: The total intensity of extragalactic background light (EBL) integrated over all sources in the universe. The horizontal axis gives the wavelength and the frequency of electromagnetic radiation, from far left to right is the Radio Background (RB), CMB, Cosmic Infrared Background (CIB),Cosmic Optical Background (COB) from stars in optical and near infrared bands, ultraviolet (UV), X-ray Background (XRB), and Gamma Ray Background (GRB) (Dole et al., 2006).

1.1.1 Diffuse Galactic emissions

The diffuse CMB foregrounds are emissions from our own Milky Way galaxy. These emissions dominate CMB contamination on angular scales $\ell \lesssim 100$, with less contribution at higher angular scales. Diffuse galactic emissions comprises of synchrotron, free-free emission and thermal emission from galactic dust. There is an additional anomalous component thought to arise from spinning galactic dust (Leitch et al., 1997).Figure 1.2 shows the frequency dependence of these components compared to the CMB. At frequencies below 60 GHz, the contamination is mainly from the synchrotron and free-free emissions. Above 60

GHz, the thermal dust is the main CMB foreground (Bennett et al., 2003; Brandt et al., 1994).

To date, modelling and removal of diffuse galactic foregrounds has been achieved. Works by (Bennett et al., 2003; Brandt et al., 1994; Hinshaw et al., 2003) reported on separating techniques of diffuse foregrounds from CMB, taking advantage of their spectral differences and morphology from the CMB signal. Full sky maps which serve as templates are now available for these foregrounds removals (Dickinson et al., 2003; Finkbeiner et al., 1999; Finkbeiner, 2003; Haslam et al., 1981; Planck Collaboration et al., 2015).

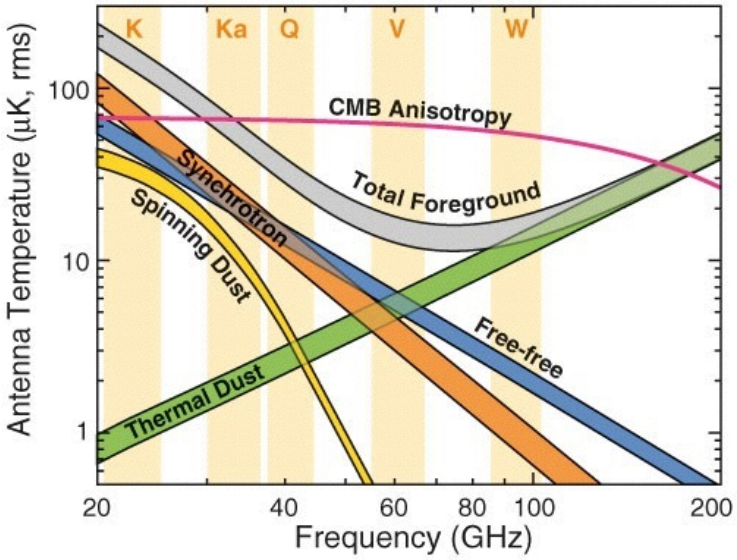

Figure 1.2: The rms anisotropy of diffuse galactic foregrounds in comparison to CMB anisotropy as a function of frequency. At lower frequencies (40 GHz), the contamination comes from synchrotron, free-free and spinning dust emissions, while the presence of thermal dust is seen at frequencies above 100 GHz (Bennett et al., 2003)

1.1.1.1 Synchrotron emission

Synchrotron radiation is emitted when relativistic particles (usually electrons) gyrate around galactic magnetic field lines, under the influence of Lorentz force. There are different as-

tronomical processes responsible for accelerating cosmic-ray electrons. In star forming galaxies (SFG), electrons are accelerated by shock waves of supernovae explosions, while in AGNs electrons are accelerated along with the relativistic jets resulting from accretion of materials onto a supermassive black hole at the centre of the galaxy (Rybicki & Lightman, 1979).

The spectrum of non-thermal synchrotron emission is described by the power law,

$$S_v \propto \nu^{-\beta} \tag{1.1}$$

where S_v is the observed flux density, ν represents the dependence of flux density on frequency and β is the spectral index. β depends on the energy distribution of relativistic electrons and is dependent on the astrophysical objects generating the synchrotron emission.

Galactic synchrotron contaminates CMB mainly at lower radio frequencies, $\sim \nu < 70$ GHz, above these frequencies it doesn't cause acute limitation to precise CMB observations. It can be separated from CMB by using templates derived from lower frequency (<2 GHz) observations, where there is no contamination from other emissions. The mostly used all sky template is the 408 MHz map presented by (Haslam et al., 1981) (shown in fig. 1.3(a). There is also 1420 MHz map by (Reich & Reich, 1986), which only covers the northern part of the sky. From these maps the derived spectral index for galactic synchrotron is reported to have values of $\beta \sim 2.8$ to 3.2 (Davies et al., 1996; Reich & Reich, 1986).

1.1.1.2 Free-Free Emission

Free-Free emission is electromagnetic radiation emitted when free electrons are scattered in the electric field of an ion in an ionized plasma. It is also commonly known from the German word *Bremsstrahlung*, which means 'braking radiation'. The frequency dependence of free-free emission is described by a power-law of the form $S_{(\nu)} \propto \nu^{-\beta}$, with spectral index $\beta \sim 2.15$ within frequencies of 1-10 GHz and varies slightly to ~ 2.13 at 100 GHz.

Free-Free emission contaminates CMB spectrum at frequencies below 100 GHz. Fre-

quency dependence of free-free is well known ($\beta \sim 2$), but because of its unknown amplitude and power spectrum, it is difficult to distinguish it from synchrotron emission using spectrum alone at radio frequencies. The Hα line produced by the same warm ionized medium responsible for free-free is rather used. Mostly used full-sky Hα template map build by (Dickinson et al., 2003; Finkbeiner, 2003) is shown by fig. 1.3(b).

1.1.1.3 Galactic Dust emission

At far-infrared and sub-millimetre wavelengths, the emission is mainly thermal radiation from interstellar dust. The infra-red emission is emitted by galactic dust grains which absorb local interstellar radiation field (LIRF) at UV-optical and re-emits it at FIR/sub-mm bands. The temperature of grains of interstellar dust (T $\sim$ 10-30 K) is related to total energy of photons in the ISFR via Stefan-Boltzmann law

$$U = \frac{4\sigma}{c} T^4, \tag{1.2}$$

where σ is Stefan-Boltzmann constant and c is the speed of light. Hence more emission results from star-forming regions where the dust is warmer due to heat from a population of newly born bright stars.

The spectrum of thermal dust emission is approximated by modified blackbody spectrum;

$$S\nu \propto \nu^{\beta} B(\nu) \tag{1.3}$$

where $B(\nu)$ is the plank function,

$$B(\nu) = 2h\nu^3 \frac{1}{exp(h\nu/kT) - 1} \tag{1.4}$$

.

The spectrum of thermal dust emission peaks between 100 and 200μm in the infrared, and its spectral index β ranges between 1.5 - 2 (Reach et al., 1995).

Diffuse thermal dust emission dominates contamination of CMB at higher frequencies (ν >100 GHz), mainly along the galactic plane, it is traced by far-infrared surveys. The

mostly used templates for diffuse thermal dust are built from combined data from Infrared Astronomy Satellite (IRAS) and Diffuse Infrared Background Experiment (DIBRE) on Cosmic Background Explorer (COBE) (Finkbeiner et al., 1999), shown in fig. 1.3(c) .

In addition to thermal dust emission, there is an Anomalous Microwave Emission (AME) or spinning dust detected at frequencies from 20GHz to 40GHz which is identified as a dust component. Its origin is not well understood, but (Draine & Lazarian, 1998) proposed the origin of this emission as the electric dipole radiation from spinning dust particles.

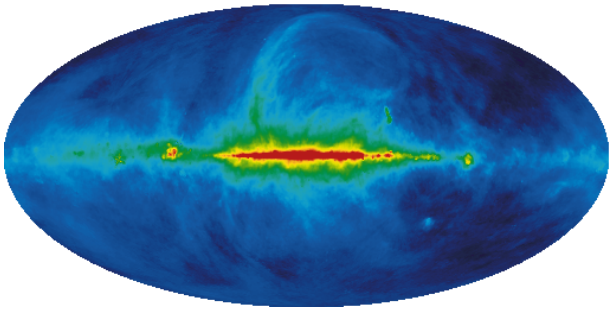

(a)

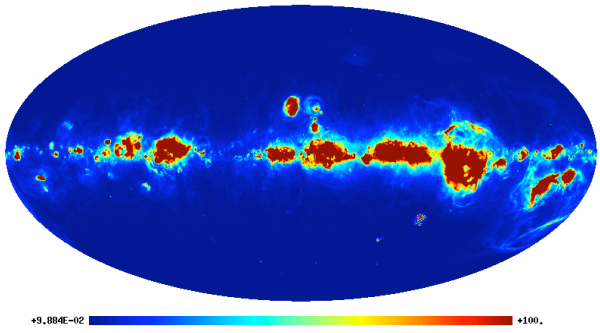

(b)

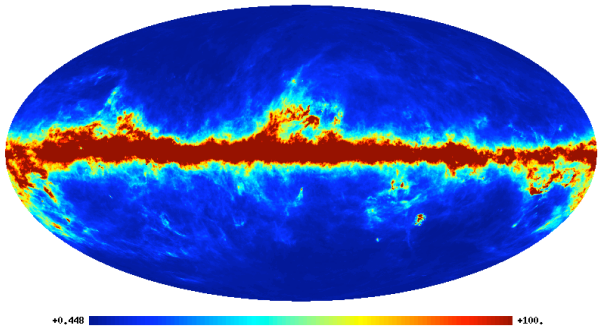

(c)

Figure 1.3: a) is the galactic synchrotron measured at 408 MHz (Haslam et al., 1981), b) is the free-free template via Hα surveys (Dickinson et al., 2003; Finkbeiner, 2003), c) is the thermal dust emission template extrapolated from 100 μm emission and 100/240 μm flux ratio maps from IRAS and COBE data (Finkbeiner et al., 1999).

1.1.2 Extragalactic point sources

The extragalactic point sources are the main source of CMB contamination towards small angular scales of $\ell \gtrsim 3000$. Figure 1.4 shows an example of CMB power spectrum measured by ACT at 148 GHz and 218 GHz, presented in (Dunkley et al., 2011).

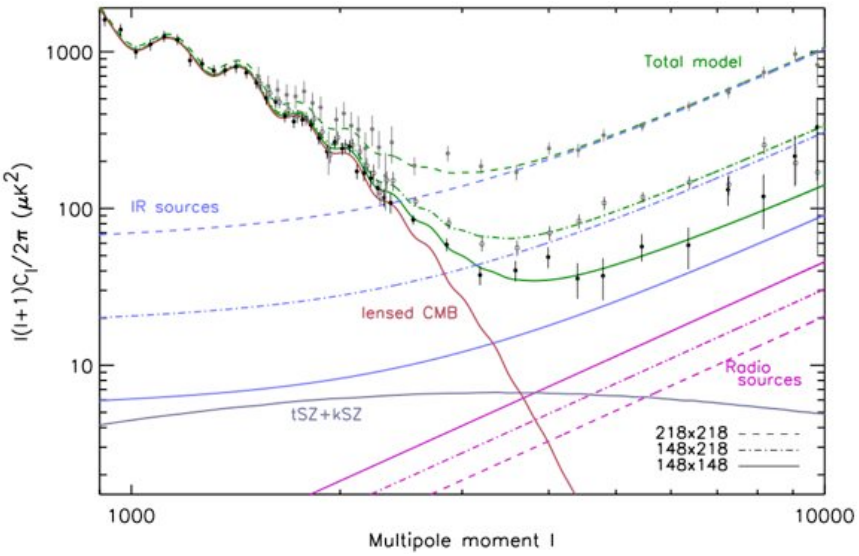

Figure 1.4: The expected angular power spectrum of ACT presented by (Dunkley et al., 2011). CMB power is dominated by power from infrared sources shown by the dashed blue line, and radio sources shown in pink colour. Extragalactic power starts dominating at higher multipoles $\ell \gtrsim 3000$. More power comes from infrared sources (DSFGs), with both Poisson and clustered terms expected to be significant. There is also contributions from thermal and kinematic SZ effects.

The power from extragalactic emissions start to dominate the Silk damping tail of CMB and continue to grow with increasing multipole ℓ (De Zotti & Toffolatti, 1998; De Zotti et al., 2015; Dunkley et al., 2013; Planck Collaboration et al., 2011; Toffolatti et al., 1998). The contamination comes from non-thermal synchrotron emitted by AGNs (Toffolatti et al., 1999) and thermal dust emission from Infrared sources (DSFGs) (Lagache et al., 2005; Marsden et al., 2014; Vieira et al., 2010). Each of these populations will be discussed in detail in the following sections. At small angular scales there is also contamination coming

from secondary anisotropies signals which will not be discussed on this study, for more reading see (Aghanim et al., 2008) for review.

1.1.2.1 Radio sources

Radio galaxies emit radio waves through non-thermal synchrotron and free-free processes, with non-thermal synchrotron being the dominant emission. The synchrotron emission emitted by radio point sources has similar spectral behaviour to the one discussed in §1.1.1.1, with a steeper spectrum, $\alpha \sim$ -0.75. The cosmic rays emitting synchrotron are powered either by AGNs or supernovae explosion. The free-free emission results from the ionised plasma of AGNs jets, whos spectral behaviour has already been discussed in §1.1.1.2.

The evolution of radio sources is well studied with low-frequency deep radio surveys (Hodge et al., 2011; Becker et al., 1995; Condon et al., 1998). Low-frequency observations are advantageous because they are not hampered by interstellar dust, making it possible to detect galaxies in dust-enshrouded distant regions which are not observable at optical wavelengths. The common way of studying flux density distribution of radio sources is through differential source counts $n(s) \equiv d(N > S)/dS$, the total number of sources in a steradian having flux density between S and $S + dS$. By assuming the simple static Euclidean universe, the flux density S of a source at distance R scales as R^{-2}, and the total number of observed sources N is proportional to the volume R^3. Thus the number of sources having density flux greater than S is given by $N(> S) \propto \mathrm{S}^{-3/2}$, and the differential source count is given by $n(s) \propto \mathrm{S}^{-5/2}$. The expected graph is horizontal for the case of constant number density with time. This is not the case, the non-Euclidean shape shown in fig. 1.5 is obtained, meaning that the number density of radio sources changes with time.

The slope of the graph indicates the change in the source population. There are two populations of sources expected to dominate the 1.4 GHz radio observations. When reading the fig. 1.5 from right to left, at flux densities around $S_{1.4GHz} \gtrsim 1$ Jy where the graph follows Euclidean shape, the counts are dominated by powerful radio sources (radio-loud AGNs

and quasars). At sub-mJy regime(< 1 mJy), the populations of the sources responsible for the flattening of the radio source counts are SFGs and radio-quiet AGNs (De Zotti et al., 2010; Ibar et al., 2009; Mitchell & Condon, 1985). The major emission from all these sources is non-thermal synchrotron radiation.

The electrons responsible for this non-thermal synchrotron from SFGs are accelerated by shock waves from supernovae remnants of young massive stars ($M > 8M_{\odot}$) within star forming regions. There is also minor thermal free-free emission from hot, ionised HII regions within star forming regions.

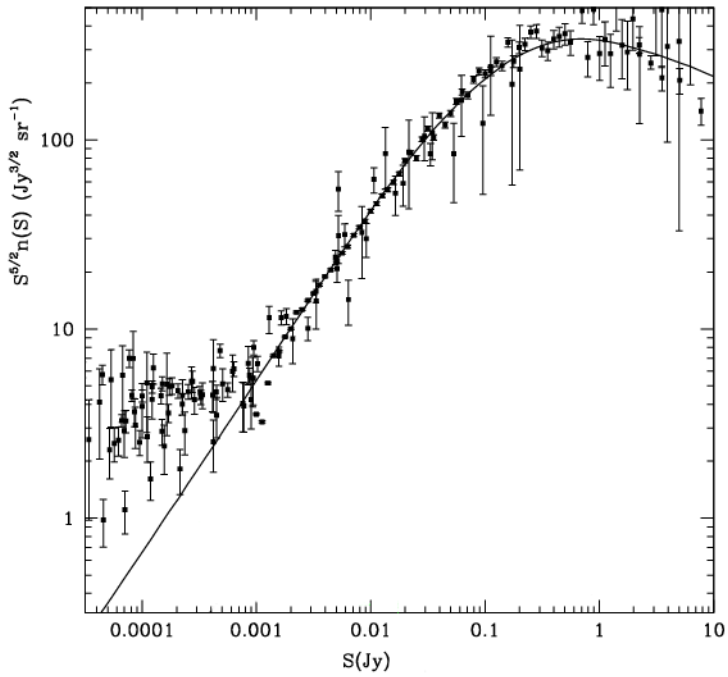

Figure 1.5: The Euclidean normalized differential radio source counts at 1.4 GHz from (De Zotti et al., 2010). At higher fluxes the source counts are expected to be dominated by radio-loud AGNs. Below 1 mJy where the graph start flattening, the source counts are dominated by radio-quite AGNs and star-forming galaxies.

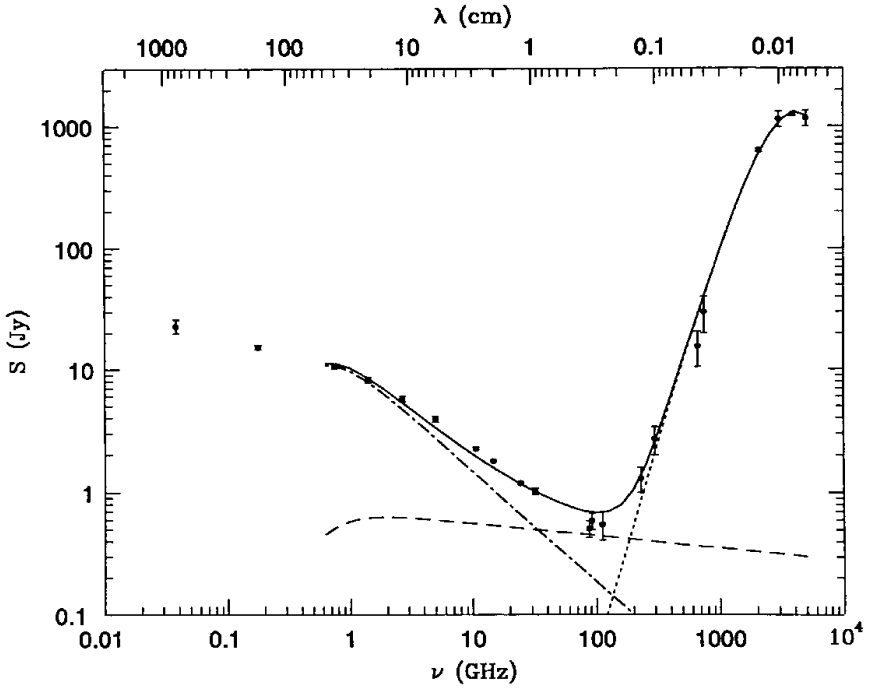

Figure 1.6: The spectrum of a star-forming galaxy, M82 from radio to far-IR frequencies. Taken from Condon (1992). The solid line represents the overall spectrum of M82, the dot-dashed line is synchrotron emission from cosmic-ray electrons accelerated by shocks from supernova explosions. The steep dotted line towards the higher frequencies is the thermal emission emitted by dust heated by UV light of young stars. The dashed line is free-free emission from hot, ionised HII regions within star forming regions that contain young stars responsible for other emissions mentioned above.

The contribution of radio foregrounds to CMB contamination is most notable at frequencies less than $v \sim 200$ GHz (Toffolatti et al., 1999). Towards higher frequencies or mm wavelength radio sources do not cause severe contamination to CMB due to steep synchrotron spectrum and energy loss by electrons, only the brightest are detected. Their Poisson distribution results in a white noise power spectrum scaled as $C_l \propto \ell^2$ and continues to grow with increasing ℓ. The clustering power term of radio sources is dominated by faint sources, therefore, its contribution to the CMB contamination is negligible, only Poisson power is expected to cause significant contamination (Toffolatti et al., 1999).

1.1.2.2 Cosmic Infrared Background

From fig. 1.1, the cosmic infrared background (CIB) contributes the next biggest fraction of the intensity of the total extragalactic background light after CMB. The CIB emission results from thermal dust, similar to the case discussed for galactic thermal dust in §1.1.1.3. The interstellar thermal dust in the star forming regions where there is a high star formation rate absorbs ultraviolet and optical energy from young stars and re-emits it at infrared wavelengths. The spectrum emitted is that of a modified blackbody spectrum, like the galactic dust. A large fraction of the CIB is believed to originate from DSFGs at higher redshift ($z \sim$ 1-4) (Fixsen et al., 1998; Puget et al., 1996).

The CIB is a major CMB contamination at small-scales, for example, at $\ell \sim 3000$ the DSFGs is almost equal the CMB power at 150 GHz (Dunkley et al., 2013; Toffolatti et al., 1998). Both Poisson and clustering power terms are expected to cause significant contamination to CMB measurements as shown in fig. 1.4, with clustering dominating Poisson power on scales less than 3 arc-minute.

1.2 Dusty-Star Forming Galaxies

This section looks in more detail at the literature of DSFGs which is the main target foreground for this study. I will outline the scant information known about these sources, along with their relationship with sources observed by low-frequency radio observations.

From their name, one can tell that they are galaxies with lot of dust undergoing intense star formation. DSFGs are well studied at far infrared and submm wavelengths. They can also be detected at submm regime of deep radio observations (De Zotti et al., 2010), and hardly seen by optical surveys because of dust absorption. They are seen by far-IR and submm surveys because the starlight from young massive stars is absorbed by the dust grains ranging from of sizes as small as a few molecules to 0.1 mm. The dust grains within the star forming then re-radiate at far-infrared and submm wavelengths (Draine, 2003). The submm observations also benefit from so-called "negative k-correction", which makes

DSFG brightness mostly independent of z, hence easier to detect (Blain et al., 2002). Since their discovery, these sources have been one of the most studied extragalactic populations (e.g.,Barger et al. (1998); Chapman et al. (2005); Coppin et al. (2008); Smail et al. (1997); Hall et al. (2010); Vieira et al. (2010)). For further reading, a detailed review of DSFGs is given by (Casey et al., 2014).

1.2.1 Local IR galaxies

To give a clear picture of high-z DSFGs, we start by a brief discussion of local luminous IR galaxies. In the 1980s Infrared Astronomy Satellite (IRAS;(Neugebauer et al., 1984)) , followed by the ISO satellite observed thousands of local galaxies (z< 1) at far-infrared and submm wavelengths. The detected selected IR-luminous galaxies by both satellites were classified as either luminous infrared galaxies (LIRGs, Sanders & Mirabel (1996); Soifer et al. (1984)) with luminosities $10^{11} < L_{IR} < 10^{12}$ $L_{\odot}$ and ultraluminous infrared galaxies (ULIRGs, (Houck et al., 1985) with 10^{12} $L_{IR} < 10^{13}$ $L_{\odot}$. These two populations were identified as the results of major mergers of gas-rich galaxies , with the IR emission believed to be powered by either starbursts or active galactic nuclei (Murphy et al., 1996).

The detection of the CIB by the Cosmic Background Explorer (COBE) satellite with the Far Infrared Absolute Spectrophotometer (FIRAS, Fixsen et al. (1998); Puget et al. (1996)), revealed that the energy emitted at infrared and submm wavelengths is roughly equal to the energy emitted at optical and ultraviolet wavelengths. Meanwhile, studies pointed out that infrared emission from local galaxies contributes only a small fraction of CIB(Soifer & Neugebauer, 1991). This implied that there might be other sources at higher-z responsible for the bulk of the CIB. Further studies revealed that indeed the high-z DSFGs are the primary source of CIB (Blain et al., 2002; Devlin et al., 2009; Lagache et al., 2005).

1.2.2 High redshift dusty galaxies

High-z DSFGs galaxies were first detected by SCUBA, the Submillimeter Common-User Bolometer Array, at wavelengths of 850μm using the James Clerk Maxwell Telescope (JCMT) (Barger et al., 1998; Hughes et al., 1998; Holland et al., 1999; Smail et al., 1997). They are well known as submillimeter galaxies (SMGs), named after their first discovery at submm wavelengths. Since their first detection by SCUBA, specialized instruments have been designed, both space-born and ground based, to study the cosmic infrared background and resolve the properties of these sources, (e.g., Spitzer-MIPS Rieke (Rieke et al., 2004), BLAST, (Devlin et al., 2009), ACT, (Marsden et al., 2014), SPT (Vieira et al., 2010), SCUBA-2 (Holland et al., 2013), Herschel,(Magnelli et al., 2012)).

Despite progress on the study of the DSFGs at higher redshifts ($z > 1$), to fully characterise their physical properties remains challenging. A major problem is a limitation brought by the spatial resolution of far-IR/submm instruments, and the dusty nature of these sources, which makes their detection at other bands difficult. The confusion-limited sensitivity of single dish instruments means that only the most luminous sources (i.e, $L_{IR} \geqslant 10^{10} L\odot$) are detected. The situation is improved by the use of statistical techniques like stacking (Zheng et al., 2006).

Some known properties of DSFGs are that they have extremely high SFRs, above 500 $M_{\odot} yr^{-1}$, with total infrared luminosity above of $10^{12} L\odot$ (Chapman et al., 2005). Their star formation is believed to be triggered by galaxy mergers and interactions (Smail et al., 2004). The spectral energy distribution (SED) of these objects can be modelled as a modified blackbody spectrum, $S_\nu \propto \nu^\beta B(\nu, T_d)$, discussed in detail in section 1.1.1.3. The spectral index β range from 1.5 to 2, and typical dust temperatures range between $T_d \sim$ 14K to 40K, and their spectrum peaks at rest-frame of 100 μm (Blain et al., 2003). DSFGs usually lie at redshifts greater than 1, with a median redshift of $z \sim 2.2$ (Chapman et al., 2003; Smail et al., 2004).

1.2.3 Lensed DSFGs

Recently, hundreds of rare and bright gravitationally lensed DSFGs have been detected by different millimeter and submmm surveys, (e.g., ACT, (Marsden et al., 2014; Su et al., 2016); Hershel,(Negrello et al., 2010); SPT (Vieira et al., 2010); Spitzer, (Ma et al., 2015)). These objects are easily detected because their faintness at near-infrared is boosted by lensing. Most of them do not have counterparts in the IRAS catalogue. They are expected to originate at higher redshifts (z $\geqslant$ 2), where gravitational lensing by foreground objects is mostly likely to happen. The gravitationally lensed DSFGs detected by Su et al. (2016) in the ACT 218 GHz equatorial map were found to have the median redshift of z=4.1, with a total infrared luminosity of $L_{IR} = 10^{13.32} L_{\odot}$, which suggest that they are strongly lensed with magnifications of 5-10.

1.2.4 Radio counterparts

It is well established that radio source counts are populated by star-forming galaxies and radio AGNs at mJy and lower flux densities (see fig. 1.5) (De Zotti et al., 2010). There is also a tight correlation between far-infrared and radio observations reported in Condon (1992). Therefore deep radio observations at 1.4 GHz have been very helpful in the study of submm high-z dust endorsed galaxies which are difficult to study at other bands due to dust obscuration.

One of the key parts of useful studies of submm-radio counterparts is the determining redshifts of high-z FIR/submm sources. Although FIR/submm observations benefit from strong negative K-correction, the inability to detect their counterparts at optical and ultraviolet bands, where redshift indicator emission lines are observed, makes it difficult to determine the redshift of high-z sources. With the help of radio counterparts, the position of these can accurately be obtained and used for searching at optical wavelengths and hence get redshifts. The search for infrared galaxies at radio wavelengths has been successful, but only to a certain redshift, ($z$$\sim$3) because radio observations do not benefit from negative K-correction like IR/submm observations.

1.2.5 Clustered DSFGs

The clustering power of DSFGs has been reported by different authors. Lagache et al. (2007) first measured angular at 160 μ using data from *spitzer* at spatial scales between $5\prime$ to $30\prime$. They measured excess power above cirrus and Poisson powers, which they interpreted as signature of galaxy clustering at $z \sim 1$. Amblard et al. (2011) and Thacker et al. (2013) used data from Herschel Multi-tiered Extra-galactic survey (HerMES),taken with the Spectral and Photometric Imaging Receiver (SPIRE) and data from Herschel Astrophysical Terahertz Large Area Survey (ATLAS) at 250, 350, and 500 μm bands and confirmed the galaxy clustering on arcminute angular scales, the galaxies were estimated to lie at $z \sim 4$.

For CMB studies, (González-Nuevo et al., 2005) made predictions of the angular power spectrum of clustered extragalactic point sources at CMB frequencies and concluded that at higher frequencies above 200 GHz the clustering signal could hamper the detection intrinsic CMB anisotropies. (Hajian et al., 2012) performed the cross-correlation between ACT and BLAST and measured 25σ significance detection of clustering DSFGs signal in the ACT CMB maps, they confirmed that the clustering term rise towards small angular scales.

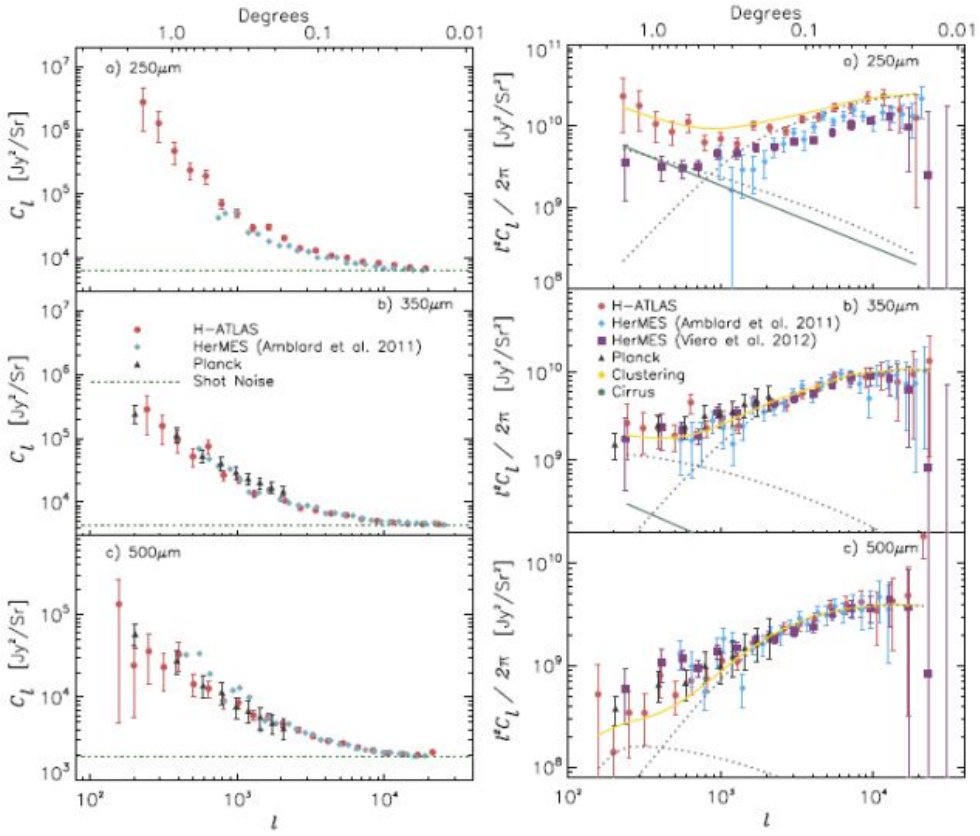

Figure 1.7: Angular power spectrum of the CIB from measurements from Herschel-ATLAS (Thacker et al., 2013), HerMES ((Hajian et al., 2012; Amblard et al., 2011)), and Planck (Planck Collaboration et al., 2014). The top is 250 μm, middle is 350 μm and bottom is 500μm bands. In the left panels, the power spectrum are plotted as C_ℓ without removal of short-noise term. In the right panels the power spectrum is plotted as $\ell^2 C_\ell/2\pi$ after removal of short noise. This figure is adopted from (Thacker et al., 2013).

1.3 The importance of this Study

This study aims at measuring the clustered power spectrum component of the DSFGs through cross-correlation between ACT and JLVA. The success of this study will enable accurate measurement of the CMB power spectrum well out on the Silk damping tail where the DSFGs play big role of contamination, hence improve measurements of CMB

parameters. This study will also present the constrains on the redshift distribution of the clustered component of DSFGs.

1.4 Overview of the Thesis

Most of the work on this study involves data reduction of the JVLA On The Fly (OTF) scan observations and the simulation of radio observations using ACT CMB maps as our models and finally the correlation between these two data sets.

The thesis is organised as follows:

- Chapter 2 presents the introduction to radio interferometry, theory of interferometric data calibration and imaging. This chapter is important for understanding the process of hands-on data reduction. This chapter also presents the literature of self-calibration that will be exercised in our data analysis process.

- Chapter 3 presents the hands-on data reduction of OTF JVLA data using CASA, starting from raw data, calibration, and finally imaging.

- Chapter 4 presents a review of the ACT telescope and its CMB measurements. It also presents the preparation process of ACT maps for cross-correlation.

- chapter 5 presents the literature of far-infrared radio correlation and the cross-correlation results.

- Chapter 6 presents the summary of the results and lay out future work.

CHAPTER 2

Theory of Radio Interferometry, Calibration and Image Synthesis

The radio data used in this thesis is acquired using an interferometer. Before going into the details of how this data was analysed, this chapter will be used to give a brief discussion of the basic concepts of radio interferometry and the theory of data calibration and imaging in radio astronomy. Most of the materials used in this chapter come from (Taylor et al., 1999) and (Thompson et al., 2001), I would recommend these textbooks for more detailed discussion on these subjects.

The first section of this chapter describes some of the basic terms from radiation laws which are applicable in radio astronomy, section 2 gives a description of radio interferometry technique, followed by the section on the theory radio interferometry data calibration and imaging.

2.1 Basic Radio Astronomy Quantities

To understand how radio telescopes measure the power of astronomical sources it is important to start by defining some of important quantities used derived from radiation laws.

2.1.1 Specific Intensity or Brightness

The energy of radiation coming from astronomical source in a direction $\boldsymbol{s}$ crossing through a detector element dA, with the bandwidth $d\nu$, into the infinitesimal solid angle $d\Omega$ in time dt, is given by equation,

$$dE = I_\nu(\boldsymbol{s})cos\theta d\Omega dA d\nu dt, \tag{2.1}$$

where θ is the angle between the incoming ray and the normal to the surface area. The quantity I_v is known as the specific Intensity (or monochromatic intensity), also known as the surface brightness of the source. I_v have the unit: $Wm^{-2}Hz^{-1}sr^{-1}$.

2.1.2 Flux density

Radio astronomers use the flux density (S) to measure the strength of radio sources. Spectral flux density ($S\nu$)is the power received per unit area, per unit frequency, obtained by integrating eq. (2.1) over the solid angle subtended by the source,

$$S_\nu = \int_{source} I_v(\theta, \phi)cos\theta d\Omega. \tag{2.2}$$

Then the flux density $\boldsymbol{S}$ is given by spectral flux intensity over the whole frequency range.

$$S = \int_{\Delta\nu} S_\nu d\nu. \tag{2.3}$$

The flux density has the units $W/m^2/Hz/sr$. Because astronomical sources have small densities, the preferred unit is called "Jansky (Jy)".

$$1Jy = 10^{-26}Wm^{-2}Hz^{-1}. \tag{2.4}$$

2.1.3 Brightness Temperature

Another important quantity in radio astronomy is the brightness temperature T_B. The intensity of a black body source in thermal equilibrium at temperature T is given by the Planck function

$$I_v(T) = \frac{2h\nu^3/c^2}{e^{h\mu/k_BT} - 1}, \tag{2.5}$$

where k is the Boltzmann's constant, h is the Plank's constant, and c is the speed of light. For the case of radio photons which have comparatively low energy, the term $hv \ll k_BT$, then the intensity $I_v(T)$ is given by the Rayleigh-Jeans approximation

$$I_v(T) = \frac{2\nu^2}{c^2} k_BT. \tag{2.6}$$

The above relation means that the brightness of blackbody emitters are directly proportional to their thermodynamic temperatures. This is a useful relation for radio astronomy, and the temperature T is defined as the brightness temperature T_B,

$$T_B = \frac{c^2}{2k\nu^2} I_v(T). \tag{2.7}$$

Radio astronomers use the brightness temperature to describe sources as if they are black body radiators. But not all radio sources are black bodies, T_B equal to the thermodynamic temperature of sources and is independent of frequency. For non-thermal emissions like synchrotron and free-free emissions which are not black body radiators, T_B can still be used, in this case it equals the temperature of blackbody that would emit the same intensity of radiation as the source, at the observed radio frequency. The flux density S is then obtained from integrating the brightness temperature over the source,

$$S = \frac{2k_B\nu^2}{c^2} \int_{source} T_B d\Omega. \tag{2.8}$$

2.2 Interferometer Fundamentals

When astronomers observe astronomical sources they are more interested in the high resolution and high sensitivity measurements. The sensitivity is the measure of faintest signal that telescope can measure and able to distinguish from background noise, while resolution is how detailed astronomers can see on the images obtained. To achieve high sensitivity and high resolution, a large collecting area is needed to collect more light from sources as much as possible. The use of radio interferometer technique plays a very important part in improvement of sensitivity and resolution of astronomical sources. In this section the radio interferometry technique is discussed and the equations used to get the sky brightness from the measured electric field are derived.

2.2.1 Single dish antenna

Starting with a single dish antenna, the angular resolution θ is given by the Rayleigh criterion:

$$\theta = 1.22\frac{\lambda}{D} \tag{2.9}$$

where λ is the observing wavelength and D is the diameter of the dish. This equation means that it will be impossible to obtain a resolution of milli-arc-seconds resolution with a single dish at radio frequencies, unless building an impractically huge telescope with a diameter above 100 km.

To solve this problem, we use radio interferometry, where the signals from a number of small telescopes are combined to act as one big telescope. The resolution from eq. (2.9) can now be calculated by replacing the diameter of telescope D with the distance between widely separated individual small telescope receivers, normally referred to as *baseline* B. With this method high angular resolution can be easily achieved while easy to maintain your antennas. Today a resolution of about Milli-arc seconds and sensitivity of few μJy have been reached, and the upcoming projects like SKA are expected to do an even better

job on sensitivity.

2.2.2 Spatial Coherence Function

In the case of more than one dish, consider the time-variable electric field $E(R,t)$ produced by the astrophysical source at position vector $\boldsymbol{R}$, the field, then propagates to receivers located point $\boldsymbol{r}$. Monochromatic radiation of this field at point $\boldsymbol{r}$ is given by,

$$E(_{\boldsymbol{r}}) = \iiint P_v(\boldsymbol{R},\boldsymbol{r}) E_v(\boldsymbol{R}) dxdydz, \tag{2.10}$$

where function $P_v(\boldsymbol{R},\boldsymbol{r})$ is the propagator, describing the influence of the electric field at position $\boldsymbol{R}$ on the electric field at position $\boldsymbol{r}$.

To simplify the above equations, a few assumptions are made. It is assumed that the space between us and the source is empty, all sources$|\boldsymbol{R}|$ are in the far field of the array, and we ignore polarisation. The eq. (2.10) then becomes,

$$E(\boldsymbol{r}) = \int \xi_v(\boldsymbol{R}) \frac{e^{2\pi i v(\boldsymbol{R}-\boldsymbol{r})/c}}{|\boldsymbol{R}-\boldsymbol{r}|} dS. \tag{2.11}$$

The field strength $E_v(\boldsymbol{R})$ is replaced by $\xi_v(\boldsymbol{R})$, the strength of electro-magnetic wave at a convenient distance from us, and dS is the element of surface on the celestial sphere.

The interferometer measures the correlation of fields from different detectors. We can now define the **spatial coherence function** between two detectors at $\boldsymbol{r_1}$ and $\boldsymbol{r_2}$ which is given by

$$V_v(\boldsymbol{r_1},\boldsymbol{r_2}) = \langle E_v(\boldsymbol{r}_1) E_v^*(\boldsymbol{r}_2) \rangle \tag{2.12}$$

where $\langle\rangle$ indicate time-averaging, and * indicate the complex conjugation. The spatial coherence function is commonly known as *visibility function*, which is the word we are going to use throughout this thesis.

Substituting eq. (2.10) in eq. (2.12), the visibility function can be written as,

$$V_v(\boldsymbol{r_1}, \boldsymbol{r_2}) = \langle \iint \xi_v(\boldsymbol{R}_1)\xi_v^*(\boldsymbol{R}_2)\frac{e^{2\pi iv(\boldsymbol{R}_1-\boldsymbol{r}_1)/c}}{|\boldsymbol{R}_1-\boldsymbol{r}_1|}\frac{e^{2\pi iv(\boldsymbol{R}_2-\boldsymbol{r}_2)/c}}{|\boldsymbol{R}_2-\boldsymbol{r}_2|}dS_1dS_2\rangle. \tag{2.13}$$

By assuming that the radiation from astronomical sources is spatially incoherent, the value of $\langle \xi_v(\boldsymbol{R}_1)\xi_v^*(\boldsymbol{R}_2)\rangle$ becomes zero for $\boldsymbol{R_1} \neq \boldsymbol{R_2}$. Then eq. (2.13) becomes

$$V_v(\boldsymbol{r_1}, \boldsymbol{r_2}) = \int \langle |\xi_v(\boldsymbol{R})|^2\rangle |\boldsymbol{R}|^2 \frac{e^{-2\pi iv(\boldsymbol{r}_1-\boldsymbol{r}_2)/c}}{|\boldsymbol{R}|^2(1-\frac{r_1}{|\boldsymbol{R}|})(1-\frac{\boldsymbol{r_2}}{|\boldsymbol{R}|})}dS. \tag{2.14}$$

The above equation can be simplified further by making assumption that the distance to the $\boldsymbol{R}$ is much greater than $\boldsymbol{r_1}$ and $\boldsymbol{r_2}$ then the values $\boldsymbol{r}/|\boldsymbol{R}|$ can be neglected. The term $dS/|\boldsymbol{R}|^2$ represents the element solid angle $d\Omega$, and unit factor $\boldsymbol{R}/|\boldsymbol{R}|$ is replaced by $\boldsymbol{s}$. The vector difference $\boldsymbol{b}$=$\boldsymbol{r_1}$ -$\boldsymbol{r_2}$ is the baseline. The term $\langle |\xi_v(\boldsymbol{R})|^2\rangle |\boldsymbol{R}|^2\rangle$ represents the observed intensity, $I_v(\boldsymbol{s})$ from an element of solid angle $d\Omega$ in the direction of $\boldsymbol{s}$. The eq. (2.14) then reduces to

$$V_v(\boldsymbol{r_1}, \boldsymbol{r_2}) = \int I_v(\boldsymbol{S})e^{-2\pi iv\boldsymbol{s}\cdot\boldsymbol{b}/c}d\Omega. \tag{2.15}$$

The

The baseline is given by $\boldsymbol{b}_{uvw}$=$(u\lambda, v\lambda, w\lambda)$. The arrays are usually in a flat surface, for most of time the w-component will be ignored and have smaller effects on the data. But this is not always the case, for lower frequency observations the third component is accounted for.

The sky brightness distribution towards different parts of the sources is describe by the (l, m, n) coordinate system also shown in fig. 2.1. Taking into consideration the brightness from a direction $\boldsymbol{s}$=$\boldsymbol{s_0}$+σ from the phase centre, the unit vector $\boldsymbol{s}$ have components $(l, m, n = \sqrt{1-l^2-m^2})$ given in terms of direction cosines with respect to the phase centre S_0.

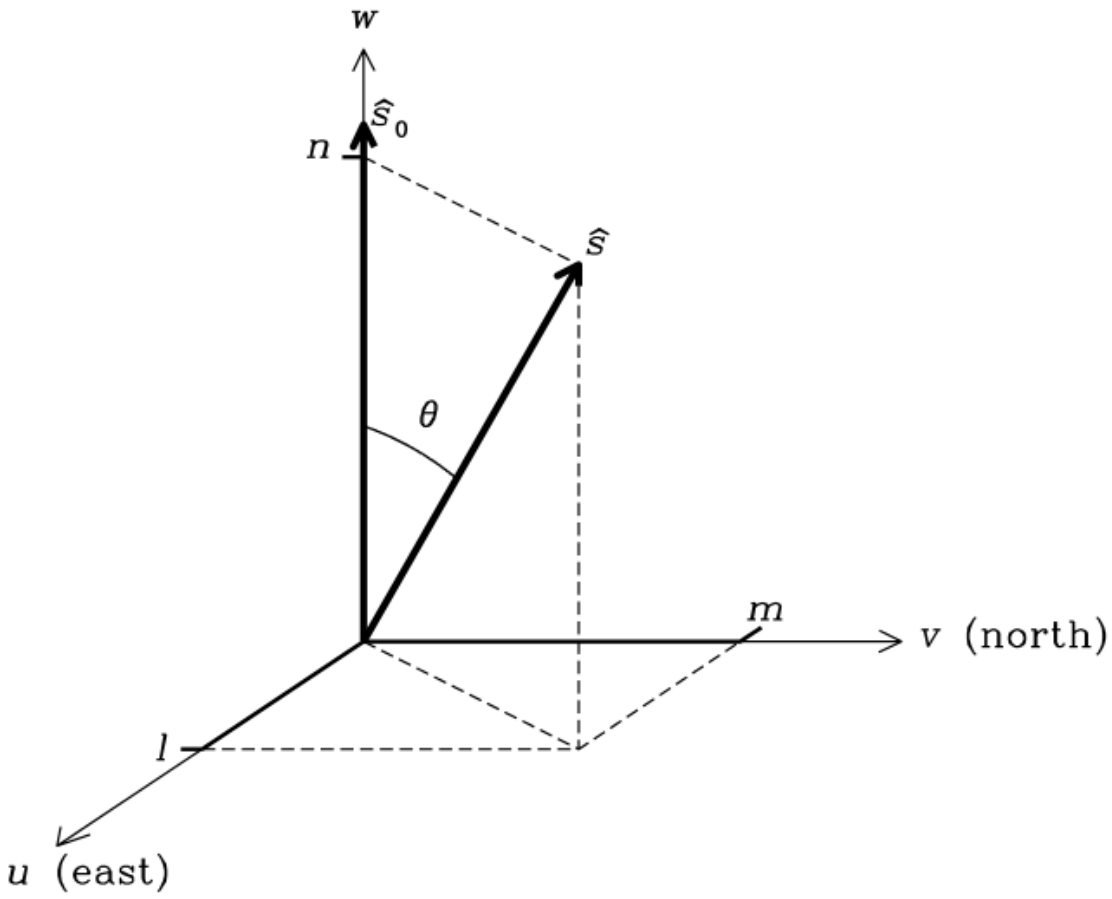

Figure 2.1: The coordinate system used in Radio interferometry : this diagram shows two different coordinates system, (a) there is uvw coordinate system used to define the baseline vector, this system have units of wavelength λ. The w-component is along the $(s_0$, the direction to the measured source. The uv-plane is perpendicular to $(s_0$. (b) The other coordinate system shown by this diagram is the lmn system which defines the 3D distribution of the source brightness around $(s_0$. The vector $\boldsymbol{s}$ is the extend distribution up-to-point s. `https://www.cv.nrao.edu/course/astr534/Interferometers2.html`

By ignoring the w-axes, the dot product from eq. (2.15) becomes,

$$\boldsymbol{s}.\boldsymbol{b}/c = ul + vm + wn = ul + vm \tag{2.16}$$

The visibility function can now be written as

$$V_v(u,v,w=0) = \int I_v(l,m) e^{-2\pi(ul+vm)} \frac{dldm}{\sqrt{1-l^2-m^2}} \tag{2.17}$$

where the solid angle $d\Omega$ in (l,m,n) coordinates represented by

$$d\Omega = \frac{dldm}{\sqrt{1-l^2-m^2}}. \tag{2.18}$$

If $|l^2+m^2|$ is very small, which is often the case, the factor $1/\sqrt{1-l^2-m^2}$ is negligible.

A simplified two-dimensional FT equation for calculating radio astronomy visibilities is now given by

$$V(u,v) = \int\int I(l,m) e^{2\pi i(ul+vm)} dldm. \tag{2.19}$$

This equation is known as $\boldsymbol{vancittert - Zernikerelation}$, who invented it from optical context. The relation means that the Fourier transform of measured visibility function gives the brightness distribution $I(l,m)$.

The interferometer measures the source flux density modified by the primary beam or the normalized reception pattern of individual antennas A(u,v), thus the visibility function is given by,

$$V(u,v) = \int\int A(l,m) I(l,m) e^{2\pi i(ul+vm)} dldm. \tag{2.20}$$

2.3 Image Synthesis

This section looks at the concepts followed to solve the inverse problem, namely to obtain the sky brightness $I(l,m)$ from $V(u,v)$.

$$A(l,m)I(l,m) = \int\int V(u,v) e^{2\pi i(ul+vm)} dudv. \tag{2.21}$$

According to above equation, to generate the complete/true sky brightness, one would have to measure the visibility function $V(u,v)$ over the entire UV-plane. Meanwhile, in practice, the UV-coverage is incomplete, since the interferometer samples discrete Fourier components (u_i, v_i) in the UV-plane. To get the complete visibility coverage, imaging algorithms must predict the missing information.

Fourier theory allows us to write the sampled visibility $\mathrm{V}^{'}(u,v)$ as the true continuous visibility $\mathrm{V}(u,v)$ multiplied by the sampling function $\mathrm{S}(u,v)$, while sampling function $\mathrm{S}(u,v)$ can be written using the two-dimensional Dirac delta function δ,

$$V^{'}(u,v) = \sum_{i=1}^{M} \omega_i \delta(u-u_i, v-v_i) V(u,v). \tag{2.22}$$

$$S(u,v) = \sum_{i=1}^{M} \omega_i \delta(u-u_i, v-v_i), \tag{2.23}$$

where the term ω_i is the weighting function, which will be explained in detail in §2.3.1.

The Fourier transform of the sampled visibilities $V^{'}(u,v)$ generates a raw image known as the dirty image $I^D(l,m)$ given by

$$I^D(l,m) = \int\int S(u,v) V(u,v) e^{2\pi i(ul+vm)} du dv. \tag{2.24}$$

Using the convolution theorem, the equation of the dirty image I^D can be written as convolution of the true sky brightness I^{true} with the point spread function (PSF). The point spread function I^{psf} is the Fourier transform of the sampling function $S(u,v)$.

$$I^D(l,m) = I(l,m) \star I^{psf}, \tag{2.25}$$

where

$$I^{psf} = \int\int S(u,v) e^{2\pi i(ul+nm)} du dv, \tag{2.26}$$

and

$$I(l,m) = \int\int V(u,v) e^{2\pi i(ul+nm)} du dv. \tag{2.27}$$

2.3.1 Visibility weighting

The weighting function ω_i is useful for modifying the shape of the PSF before transforming visibilities to the sky plane. The choice of weighting function depends on one's interest. For maximum point source sensitivity (low rms in the image) and hence best detection of low signal to noise sources, *natural* weighting is used. It is given by

$$w_i = \frac{1}{\delta_i^2}, \tag{2.28}$$

where δ^2 is the noise variance of the data. Natural weighting gives equal weight to all different sampled points. Generally it gives more weight to low spatial frequencies than high spatial frequencies since more the visibility density is usually higher on short baselines than long ones, resulting in poor angular resolution.

For higher resolution $uniform$ weighting can be used. Uniform weighting give all spatial-frequencies in a grid cell uniform weight. If there is $\rho(u, v)$ number of sampled points in a (u,v) cell then the weight for each point would be

$$w_i = \frac{1}{\rho(u_i, v_i)}. \tag{2.29}$$

This would lower the beam side lobes and enhance angular resolution by giving more weight to high spatial frequencies, but degrades the point source sensitivity.

To improve the resolution without losing too much point source sensitivity relative to natural weighting, *robust* weighting can be used. Robust weighting generates a dirty beam by combining natural and uniform weighting. For this work robust weighting will be used for imaging.

2.3.2 Gridding

The transformation of visibilities into dirty image presented by eq. (2.17) can be done in two ways. The first method is through direct Fourier transform (DFT), which sums all sampled M visibilities:

$$I^D = \frac{1}{M} \sum_k V(_{u_i,v_i)} e^{2\pi i(u_i l + v_i m)} \tag{2.30}$$

DFT of M non-regularly sampled points will take $\mathcal{O}(M^2)$ steps, making it difficult to perform on observations from large arrays and for long observations where M can reach order of millions, therefore this method is rarely used.

The other method is the Fast Fourier Transform (FFT). FFTs are more efficient - they can compute the DFT in $\mathcal{O}(n \log n)$ steps. For FFT algorithm to work, the visibilities need to be interpolated onto a rectangular grid of cells. This process is known as gridding and can be done easily with imaging software.

The grid size is estimated from the primary beam. For imaging to work well the image should be at least 3 times primary beam. The cell size was then obtained from synthesized beam calculated using the equation

$$\theta = \frac{\lambda}{D} = \frac{1}{uv_{max}} radians = \frac{3600x180}{\pi u_{max}} arcsec. \tag{2.31}$$

where uv_{max} is the maximum uv-distance (in Kλ) which can be obtained from plot of visibilities. To obtain good image the cell size is estimated to be four or five times less than the synthesised beam.

2.3.3 Deconvolution

In radio interferometry imaging there are different deconvolution algorithms available for deconvolution of the sky from the PSF as shown by eq. (2.25). Hogbom CLEAN (Cornwell, 2008; Högbom, 1974) and The Maximum Entropy Method (MEM)(Cornwell & Evans, 1985; Sault, 1990) are among the commonly used deconvolution algorithms. In this work the Hogbom CLEAN will be used.

CLEAN consists of the following steps,

1. Generate dirty image and empty model image.

2. Locate the brightest pixel on the dirty image and assume that is a point source. Add these flux points to the model image.

3. Subtract model from data, leaving residuals.

4. Repeat step 2 and 3 until no bright sources are left on the dirty image, what left is the residual image.

5. Final image is obtained by convolving the model image with a restoring Gaussian "CLEAN beam" and add the last residual map to present the noise.

6. Generate dirty image and PSF.

7. Initialize residual map to dirty image and the create empty model.

8. Locate the brightest pixel on the residual map and assume that is a point source

9. Subtract some scaled fraction of the dirty beam response at this position and repeat the same process many times until there is only noise left in the residual map.

10. The final clean image is generated by convolution by clean beam.

2.4 Calibration

The previous section addressed the process of turning the visibilities into images, but before this process the observed visibilities should be corrected for errors brought by different factors on the incoming signal, among them are atmospheric attenuation, antenna pointing offsets, signal delay in the antenna instrumentation, gain changes in the electronics, correlator malfunctions, radio interference, among others. The process of correcting these errors is known as *calibration*. Calibration is a very important part of radio interferometry data reduction, as it holds the key to the synthesis of true sky brightness. Basically, what it does is to precisely estimate gains brought by the mentioned factors and correct the

visibility. In this section we give a brief overview of gain calculations. Most of the notes used in this section were obtained from (Fomalont & Perley, 1999; Bignell & Perley, 1986).

The interferometric system is designed such that is linear and the response associated with a pair of antennas does not depend on another antenna pair. The relation between measured visibilities $\tilde{V}_{ij}$ and true visibilities V_{ij} can then be expressed by the "calibration equation":

$$\tilde{V}_{ij}(t) = G_{ij}(t)V_{ij}(t) + \epsilon_{ij}(t) + \mu_{ij}(t), \tag{2.32}$$

where (i, j), represents the pair of antennas i and j, t is the time of observation, G_{ij} is the baseline-based complex gain, ϵ_{ij} is a baseline-based complex offset, and μ_{ij} is baseline complex noise resulting from thermal fluctuations of receivers. The intention of calibration is to determine the amplitude and phase complex gains G_{ij}, assuming that the off set ϵ_{ij} and the noise μ_{ij} terms are negligible.

2.4.1 Standard Calibration

One common method of estimating the complex gains G_{ij} is the standard calibration technique. Standard calibration uses astronomical calibrator sources as a reference to calculate gains. The calibrator sources are normally well studied, very bright sources, with precisely known sky positions and flux densities S. These sources are isolated from confusion noise, therefore their true visibilities V_{ij} are well known. By observing calibrator source, G_{ij} can be calculated from V_{ij} and S for each of the N (N-1) /2 different baselines, where N is the total number of antennas. If the calibrator is unresolved then the visibility is constant for all baselines at the centre of the field. This is because the size of the source is smaller than the angular resolution on each baseline.

$$G_{ij} = \frac{V_{ij}(t)}{S} \tag{2.33}$$

Because the signal is mostly corrupted by atmosphere above or electronics faults of individual antennas, the baseline based gains G_{ij} can be represented in terms of product of individual antenna-based gains g_i and g_j. The calibration equation then takes the form

$$G_{ij} = g_i(t)g_j*(t)g_{ij}(t) = a_i(t)a_j(t)a_{ij}e^{i(\phi_i(t)-\phi_j(t)+\phi_{ij}(t))}, \tag{2.34}$$

where, $a(t)$ and $\phi(t)$ are respectively the amplitude and phase antenna-based gains, and g_{ij}, a_{ij} and ϕ_{ij} are baseline-based residual gains. The residual gains are normally very small for a good system. The process of going from baseline-based to antenna-based gains have diverse advantages, firstly the computing power to reduce gains is reduced because there are fewer antennas than baselines for any array made out more than 3 antennas. Another important advantage is that the gain solutions can still be derived for all antennas even when the data from other baselines is missing. Calibrator source just needs to be unresolved at long baselines.

2.4.2 Self-Calibration

Normally after imaging corrected visibilities obtained using standard calibration, some residual calibration errors will exist in the resulting image. These are due to the amplitude and phase errors from the standard calibration. The derivation of gains $g(t)'s$ strictly from calibrators tends to be insufficient because of various reasons; firstly the variation on the troposphere and ionosphere with time makes it difficult to derive gains from different sources at different time for different directions on the sky. The other problem arises from shortage of strongly unresolved calibrator sources near the target and practically speaking there's no such a thing as an isolated point source like we assume calibrators sources are . The other main source of error result from antenna pointing errors, the error that results because antennas are pointing at wrong location than the desired one. Pointing errors results from antennas sagging, atmospheric refraction effects on antennas, misalignment of antennas rotation axes, among others.

If the imaged objects have enough signal-to-noise (S/N), complex gains can be calibrated as a function of time using the model of the target source itself. This process is known as self-calibration. Self-calibration involves using least-squares to minimize the difference R between the true visibilities $\tilde{V}$ and the model visibilities obtained from the model

image created during imaging(Cornwell & Fomalont, 1989).

$$R = \sum w_{i,j} \left(V_{ij}(t_k) - g_i(t_k) g_j * (t_k) . V_{ij}^M(t_k) \right)^2 , \tag{2.35}$$

where $w_{i,j}$ are the data weights, $g_i(t_k)g_j * (t_k)$ are the complex gains and $V_{ij}^M(t_k)$ are the model visibilities.

Self-calibration can have both advantages and disadvantages. The advantages of self-calibration is that the gains are derived for correct time and pointing, and the solutions are robust for many baselines. The disadvantages are that it might fail if there is not enough signal to create a good model, and that any artefacts in the model will lead to incorrect visibilities.

Self-calibration works as follows;

- Make an initial image (using clean) to create a source model .
- Solve antenna gains over some averaging time interval (t) using eq. (2.36).
- Deduce corrected visibility

$$V_{ij,corr}(t) = \frac{V_{ij}(t)}{g_i(t) g_j^*(t)}, \tag{2.36}$$

- Use the recalibrated data to produce a new image to generate an improved model.
- Repeat steps 2 to 5 until satisfied with noise on the image.

CHAPTER 3

JVLA Observations and Data Analysis

In this chapter we present the hands-on data reduction of Jansky Very Large Array (JVLA) observations, from raw data up to imaging. Data analysis was performed using standard routines in the Common Astronomy Software Applications (CASA) package.

CASA is software designed for radio interferometer data analysis. CASA was developed by the National Radio Astronomy Observatory (NRAO) as a successor to the Astronomical Image Processing System (AIPS), which has been actively used for radio interferometer data reduction for over 20 years. AIPS and AIPS++ use C and C++ languages, while CASA uses the core libraries of these two and the tools and tasks have python interface. This software can be obtained freely from the NRAO website `http://casa.nrao.edu/casa_obtaining.shtml`.

3.1 JVLA Observations

The radio data used for this study was taken using the Karl.Jansky Very Large Array (JVLA) /Expanded Very Large Array (EVLA) shown by fig. 3.1. JVLA is an NRAO radio

telescope located outside of Socorro, New Mexico in the USA. This telescope is one of the biggest and most sensitive radio telescopes in the history of radio interferometry. It consists of 27 identical antennas with 25-meter diameter arranged in a Y-shape. One thing that makes JVLA is that its antennas can be moved. The baselines of the array span lengths from 0.035 kilometres to 36.4 kilometres and create four primary configurations A, B, C and D with maximum baselines of 36.4 km, 11.1 km, 3.4 km and 1.0 km, respectively. The array operates at frequencies between 58 MHz to 50 GHz, divided into 10 bands.

Figure 3.1: The JVLA telescope.`https://www.nrao.edu/archives/Timeline/VLA-D_lo.shtml`

Our data were taken with the JVLA in its compact "D" configuration, using L-band with a centre frequency of 1400 MHz. The data have a bandwidth of 1024 MHz with eight sub-bands, each divided into 64 channels and contain both cross and linear polarisations. The observed field is centred at J2000 00h41m00.0 0d0m0.0, covering 12.5 deg x 3 deg ($\sim$ 37.5sq.deg). This field was chosen to overlap with the ACT equatorial strip (Dünner et al., 2013). Alongside the target source, the calibrator sources for flux, bandpass, and phase calibration (3C48 and J2253+1608, and J0022+0014 respectively) were also observed to be used in the calibration process. The observation was taken using on-the-fly (OTF) scan

technique. This technique is explained in more details in the following section §3.1.1.

3.1.1 On-the-fly Mapping

On-the-fly mapping is one of the ongoing JVLA observing techniques under development for conducting large surveys. The technique is different from the usually used scan techniques used to construct large sky mosaics, like pointing and tipping (Cornwell, 1988). OTF scanning is different in that the data is collected while the telescope beam is allowed to constantly drift between two points on the sky. The beam is allowed to move linearly with constant speed, starting from east to west, then return back from west to east with different phasecenter, creating stripes as shown in fig. 3.2. This is done by defining the RA and Dec. (J2000) of the beginning and ending of the strips. This technique is efficient to cover a large area of sky quickly. More information about OTF scan can be seen on the NRAO website `https://science.nrao.edu/facilities/vla/docs/manuals/opt/otf`.

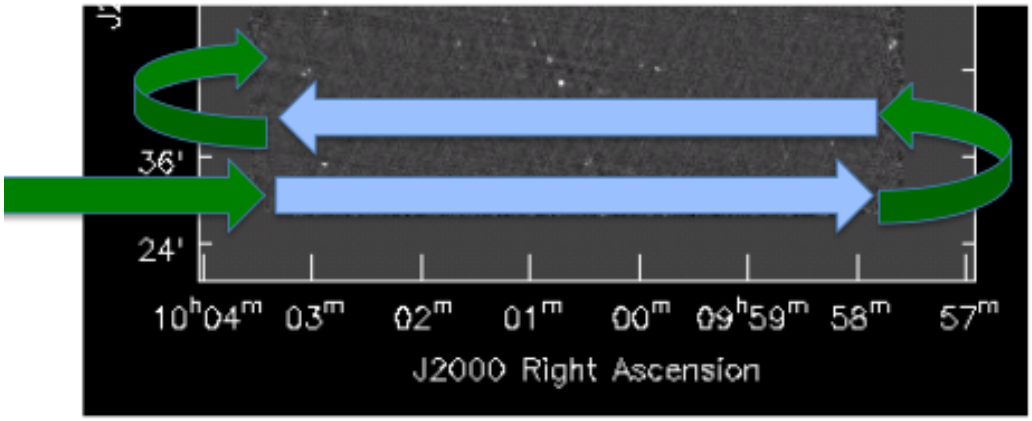

Figure 3.2: Illustration of how an OTF scan works. The telescopes scans from west to east making a stripe with fixed Dec and changing RA, then returns back to complete another stripe, and so on.

3.2 OTF Data reduction with CASA

Before going through data analysis steps, I will list some of the most commonly used tasks when analysing data using CASA.

- *plotms*: used for plotting visibilities.
- *plotants*: used for plotting antenna configuration.
- $flagdata$: used to delete unwanted data.
- *gencal*: used for correction of known antenna positions, gain curve and opacity.
- $setjy$: used for scaling the flux of primary calibrator.
- *gaincal*: used to calibrate variations of amplitudes and phases with time.
- *bandpass*: used for calibration of variations of amplitudes and phases with frequency.
- $Fluxscale$: used to transfer flux scale to other calibrator sources.
- *plotcal*: used for plotting calibration solutions.
- *applycal*: used to apply calibration solutions to data.
- *split*: used to split corrected data and raw data set.

CASA stores observed visibilities in files known as Measurement Sets (MS), widely referred to as MS files. An MS file will mostly have two columns, the data column, which stores the original data set, and remains untouched during calibration steps, and the "corrected" data column which is created when manipulating data.

3.2.1 Data Examining

The first step of data reduction is to extensively examine the observed visibilities for obvious errors that can be caused by broken antennas, antenna shadowing, correlator

malfunctions and Radio Frequency Interference (RFI). To look inside the MS file, the CASA task LISTOBS is used. LISTOBS displays measurements in a CASA logger as shown in fig. 3.3. Among the displayed information is date of observations and total time of observation, number of SPWs, and the observed fields etc.

Another important set of information worth looking at as part of examining data can be obtained from the operator's log. The operator's log gives the inside story of what happened during the observation period. It outlines important information, like weather conditions, names of dead receivers, and a list of antennas which lost positions during observations, etc.

```
================================================================================
           MeasurementSet Name:  /home/onkz/act_region/3rdfile/11B-203_sb6594961_1.55917.962341770835.ms      MS Version 2
================================================================================
    Observer: Dr. Steven T. Steven Myers     Project: uid://evla/pdb/4985810
Observation: EVLA
Data records: 18642000       Total elapsed time = 7195 seconds
    Observed from   22-Dec-2011/23:05:52.0   to   23-Dec-2011/01:05:47.0 (UTC)

    ObservationID = 0         ArrayID = 0
  Date        Timerange (UTC)          Scan  FldId FieldName             nRows     SpwIds   Average Interval(s)    ScanIntent
  22-Dec-2011/23:05:52.0 - 23:06:50.0     1      0 J2253+1608             150800  [0,1,2,3,4,5,6,7]  [1, 1, 1, 1, 1, 1, 1, 1] [CALIBRATE_AMPLI#UNSPECIFIED,
             23:06:51.0 - 23:07:50.0     2      0 J2253+1608             153400  [0,1,2,3,4,5,6,7]  [1, 1, 1, 1, 1, 1, 1, 1] [CALIBRATE_AMPLI#UNSPECIFIED,
             23:07:51.0 - 23:08:50.0     3      0 J2253+1608             153400  [0,1,2,3,4,5,6,7]  [1, 1, 1, 1, 1, 1, 1, 1] [CALIBRATE_AMPLI#UNSPECIFIED,
             23:08:51.0 - 23:09:50.0     4      0 J2253+1608             153400  [0,1,2,3,4,5,6,7]  [1, 1, 1, 1, 1, 1, 1, 1] [CALIBRATE_AMPLI#UNSPECIFIED,
             23:09:50.0 - 23:10:49.0     5      0 J2253+1608             153400  [0,1,2,3,4,5,6,7]  [1, 1, 1, 1, 1, 1, 1, 1] [CALIBRATE_AMPLI#UNSPECIFIED,
             23:10:50.0 - 23:11:49.0     6      0 J2253+1608             153400  [0,1,2,3,4,5,6,7]  [1, 1, 1, 1, 1, 1, 1, 1] [CALIBRATE_AMPLI#UNSPECIFIED,
             23:11:50.0 - 23:12:49.0     7      0 J2253+1608             153400  [0,1,2,3,4,5,6,7]  [1, 1, 1, 1, 1, 1, 1, 1] [CALIBRATE_AMPLI#UNSPECIFIED,
             23:12:50.0 - 23:13:49.0     8      1 J0022+0014             153400  [0,1,2,3,4,5,6,7]  [1, 1, 1, 1, 1, 1, 1, 1] [CALIBRATE_PHASE#UNSPECIFIED]
             23:13:50.0 - 23:14:49.0     9      1 J0022+0014             153400  [0,1,2,3,4,5,6,7]  [1, 1, 1, 1, 1, 1, 1, 1] [CALIBRATE_PHASE#UNSPECIFIED]
             23:14:50.0 - 23:15:49.0    10      1 J0022+0014             153400  [0,1,2,3,4,5,6,7]  [1, 1, 1, 1, 1, 1, 1, 1] [CALIBRATE_PHASE#UNSPECIFIED]
             23:15:49.0 - 23:16:48.0    11      1 J0022+0014             153400  [0,1,2,3,4,5,6,7]  [1, 1, 1, 1, 1, 1, 1, 1] [CALIBRATE_PHASE#UNSPECIFIED]
             23:16:49.0 - 23:16:51.0    12      2 StartScan-50.1           5200  [0,1,2,3,4,5,6,7]  [1, 1, 1, 1, 1, 1, 1, 1] [OBSERVE_TARGET#UNSPECIFIED]
             23:16:52.0 - 23:16:56.0    13      3 OTFDUMMY                10400  [0,1,2,3,4,5,6,7]  [1, 1, 1, 1, 1, 1, 1, 1] [UNSPECIFIED#UNSPECIFIED]
             23:16:56.0 - 23:17:08.0    14      4 0016000-004959          31200  [0,1,2,3,4,5,6,7]  [1, 1, 1, 1, 1, 1, 1, 1] [OBSERVE_TARGET#UNSPECIFIED]
             23:17:08.0 - 23:17:20.0    15      5 0016120-004959          31200  [0,1,2,3,4,5,6,7]  [1, 1, 1, 1, 1, 1, 1, 1] [OBSERVE_TARGET#UNSPECIFIED]
             23:17:20.0 - 23:17:32.0    16      6 0016241-004959          31200  [0,1,2,3,4,5,6,7]  [1, 1, 1, 1, 1, 1, 1, 1] [OBSERVE_TARGET#UNSPECIFIED]
             23:17:32.0 - 23:17:44.0    17      7 0016362-004959          31200  [0,1,2,3,4,5,6,7]  [1, 1, 1, 1, 1, 1, 1, 1] [OBSERVE_TARGET#UNSPECIFIED]
             23:17:44.0 - 23:17:56.0    18      8 0016483-004959          31200  [0,1,2,3,4,5,6,7]  [1, 1, 1, 1, 1, 1, 1, 1] [OBSERVE_TARGET#UNSPECIFIED]
             23:17:56.0 - 23:18:08.0    19      9 0017004-004959          31200  [0,1,2,3,4,5,6,7]  [1, 1, 1, 1, 1, 1, 1, 1] [OBSERVE_TARGET#UNSPECIFIED]
             23:18:08.0 - 23:18:20.0    20     10 0017125-004959          31200  [0,1,2,3,4,5,6,7]  [1, 1, 1, 1, 1, 1, 1, 1] [OBSERVE_TARGET#UNSPECIFIED]
             23:18:20.0 - 23:18:32.0    21     11 0017246-004959          31200  [0,1,2,3,4,5,6,7]  [1, 1, 1, 1, 1, 1, 1, 1] [OBSERVE_TARGET#UNSPECIFIED]
             23:18:32.0 - 23:18:44.0    22     12 0017367-004959          31200  [0,1,2,3,4,5,6,7]  [1, 1, 1, 1, 1, 1, 1, 1] [OBSERVE_TARGET#UNSPECIFIED]
             23:18:44.0 - 23:18:56.0    23     13 0017488-004959          31200  [0,1,2,3,4,5,6,7]  [1, 1, 1, 1, 1, 1, 1, 1] [OBSERVE_TARGET#UNSPECIFIED]
             23:18:56.0 - 23:19:08.0    24     14 0018009-004959          31200  [0,1,2,3,4,5,6,7]  [1, 1, 1, 1, 1, 1, 1, 1] [OBSERVE_TARGET#UNSPECIFIED]
             23:19:08.0 - 23:19:20.0    25     15 0018130-004959          31200  [0,1,2,3,4,5,6,7]  [1, 1, 1, 1, 1, 1, 1, 1] [OBSERVE_TARGET#UNSPECIFIED]
             23:19:20.0 - 23:19:32.0    26     16 0018251-004959          31200  [0,1,2,3,4,5,6,7]  [1, 1, 1, 1, 1, 1, 1, 1] [OBSERVE_TARGET#UNSPECIFIED]
             23:19:32.0 - 23:19:44.0    27     17 0018372-004959          31200  [0,1,2,3,4,5,6,7]  [1, 1, 1, 1, 1, 1, 1, 1] [OBSERVE_TARGET#UNSPECIFIED]
             23:19:44.0 - 23:19:56.0    28     18 0018493-004959          31200  [0,1,2,3,4,5,6,7]  [1, 1, 1, 1, 1, 1, 1, 1] [OBSERVE_TARGET#UNSPECIFIED]
             23:19:56.0 - 23:20:08.0    29     19 0019014-004959          31200  [0,1,2,3,4,5,6,7]  [1, 1, 1, 1, 1, 1, 1, 1] [OBSERVE_TARGET#UNSPECIFIED]
             23:20:08.0 - 23:20:20.0    30     20 0019135-004959          31200  [0,1,2,3,4,5,6,7]  [1, 1, 1, 1, 1, 1, 1, 1] [OBSERVE_TARGET#UNSPECIFIED]
```

Figure 3.3: Example of logger display.

As part of preparing for the calibration process, an antenna to be used as a reference should be selected. Antenna configurations can be inspected by running the CASA task PLOTANTS which then returns the array configuration shown in fig. 3.4. A good reference antenna is typically one positioned towards the centre of the array configuration, with less corrupted baselines .

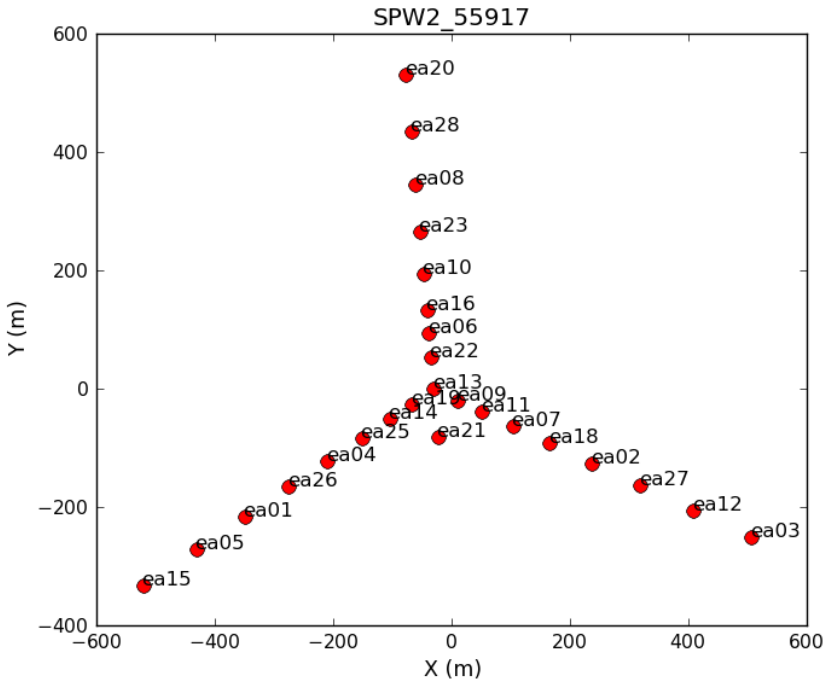

Figure 3.4: JVLA D antenna configuration

3.2.2 Prior calibration and flagging

Before the main calibration, it is necessary to correct some known errors and remove bad data which cannot be fixed. Including this data in any calibration steps would introduce errors to the final derived solutions. The following are some of the important calibration and flagging steps that should be done before the main calibration;

Antenna position correction

Because the JVLA antennas are periodically moved into different configurations, it is very important for one to correct the antenna positions before going through the main calibration steps. From eq. (2.17) we have seen that visibilities depend on antenna positions, so any errors in antenna positions will result in wrong calculations of UV-coverage, hence errors in the final synthesised sky brightness.

From the observer's log, one can get information about the antennas which had position

errors during observations. These errors can be corrected by running task GENCAL, with sub-parameter $caltype =' antpos'$. The GENCAL will fetch correct antenna positions online (from NRAO's files) and write them into the calibration file, which is then applied to the data.

Gaincurve and opacity correction

Gaincurve correction is the correction for elevation-dependence antenna gains that results from sagging and deformation of reflectors as the gravity deforms the surface of the earth. Gaincurve solutions are derived by the task GRNCAL with parameter *caltype* set to $gceff$. The opacity corrections were skipped for our data analysis; at lower frequencies this effect is very small.

Flagging dead and shadowed antennas

From the observers log, we already know which antennas were not operating during the observation. For example, it was pointed out that some antennas had an L band receiver removed for maintenance, some had circuit faults, and had corrupted data, etc. These antennas were flagged from the start by specifying them when running the CASA task FLAGDATA. During observations, some antennas can block or shadow others, these data can be flagged by running FLAGDATA with parameter $mode = shadow$.

3.2.3 RFI Flagging

Radio frequency interference (RFI) is among the main factors corrupting radio data, especially at lower frequency band like L-band. RFI signals are terrestrial or generated by human activities. The RFI can generally be easily identified on the data as it appears in the form of sharp spikes when plotting the amplitude of the data as a function of frequency. Figure 3.5 shows RFI in the raw data used for current data, the colours reflect different spectral windows (SPWs). It can be clearly seen that some of SPWs are totally wiped by RFI. In this study I restricted analysis to 2 of the cleanest SPWs. The most affected SPWs were ignored, but others which can be cleaned will be used for further studies of this project. To investigate how efficient of automatic RFI flagging can work on most RFI

affected SPWs, SPW2 was used as an example.

The CASA task *plotms* is used to plot visibilities. PLOTMS is capable of plotting different options for the axes of the data. In searching for bad data like RFI and corrupted baselines, plotting amplitude v.s. frequency and amplitude v.s. baseline is advisable.

RFI flagging is normally done manually. In CASA, the FLAGDATA parameter *mode* is set to *manual* and the data are inspected by eye while noting the data affected by RFI. For high volumes of data and strongly affected data like some other SPWs shown by fig. 3.5, it becomes difficult to go through all the data and specify RFI affected data, so manual flagging becomes very painful and time consuming. The alternative way is to use automatic flagging discussed in §3.2.3.1.

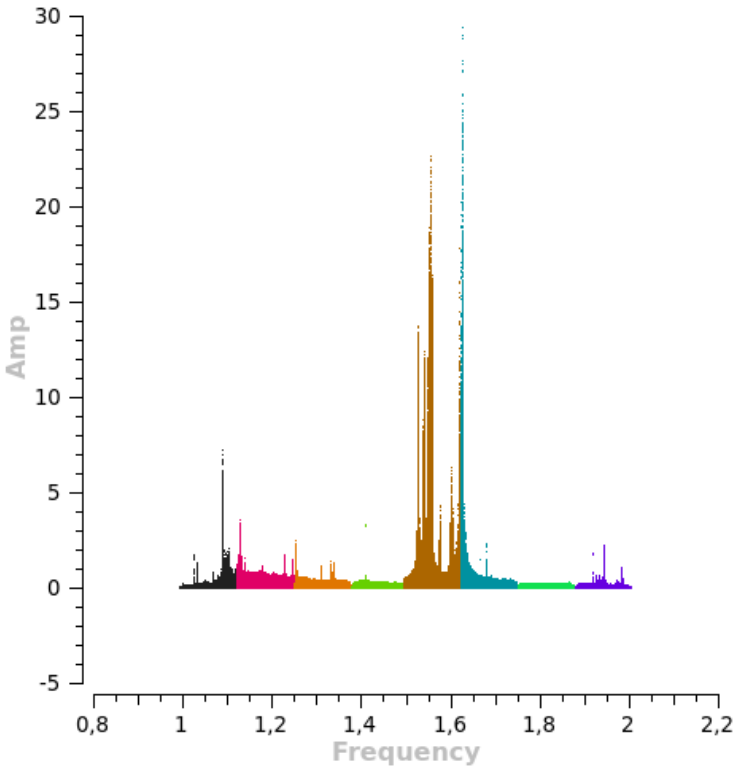

Figure 3.5: Snapshot of RFI in our raw data. Different colours represent SPWs and the data is not averaged over time.

3.2.3.1 Automatic RFI flagging

Automatic RFI flagging is different from manual flagging. The affected data are not specified by hand throughout the flagging process, RFI will instead be flagged automatically. This method is much quicker than manual flagging, but manual flagging has been shown to have better outcomes than auto flagging.

In this work, we exercised RFI flagging manually and automatically. For less affected spectral windows (SPW3 and SPW6) we used manually flagging only. The auto-flagging was tested only on SPW2. Automatic RFI flagging was performed as follows;

- **Hanning-smooth data**; First the task **hanningsmooth** was executed to Hanning smooth the data to reduce the ringing resulting from strong RFI across the band. This task improves the chances of deleting more bad data.

- **Preliminary bandpass calibration**; For best results in automatic RFI flagging, we performed pre-bandpass calibration using our phase calibrator only, this calibration was then cleared when starting the main calibration. Phase calibrator is observed multiple times through the observation, using it to make average bandpass of the observation will mitigate the amount of the RFI in the calculated bandpass.

- **run flagadata, mode=rflag**; After applying bandpass solutions to the data, automatic flagging was done by running FLAGDATA with parameter $mode = rflag$. $rflag$ detect outliers (RFI) based on sliding-window RMS filters. For each channel it calculates the local RMS of real and imaginary parts of visibilities within a sliding time window, then calculate the median RMS across time windows, deviations of local RMS from this median, and the median deviation. It then flag if local RMS N x (median RMS + median deviation). For spectral analysis (for each time step), rflag calculates the average of real and imaginary parts of visibilities and their RMS across the channels, then calculate the deviation of each channel from this average, and the median-deviation. It then flag data if deviation N x median deviation.

  The amount of data flagged is controlled by setting sub-parameters *timedevscale*

and *freqdevscale* or N which are the threshold scaling for time and spectral noise estimates. Initially both scales have default value of 5 sigma. For my data I used timedevscale and freqdevscale of 4.0, this value was enough to get rid of worst RFI on my SPW2, and the residual RFI was flagged manually. The results of automatic RFI flagging done on SPW2 are shown in fig. 3.9.

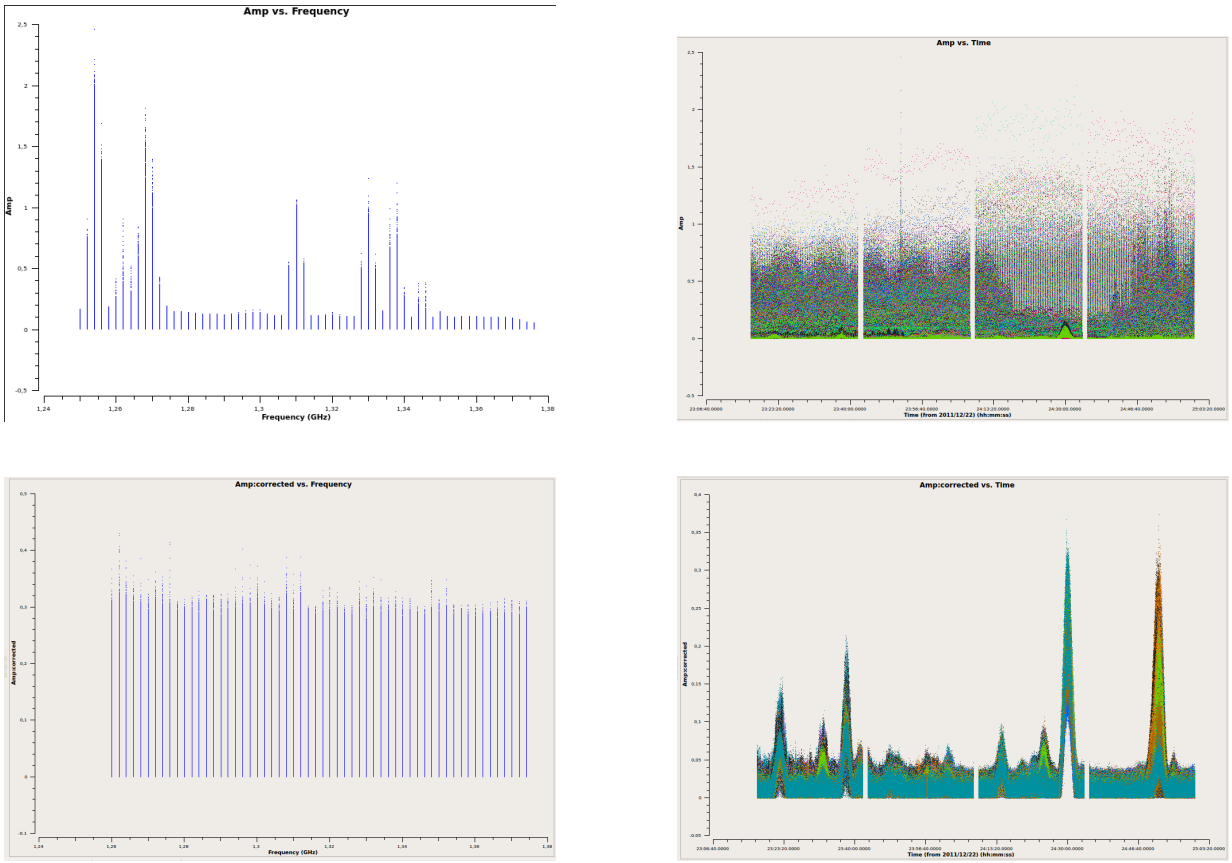

Figure 3.9: How the amplitude vs time graph of science target looks like after flagging bad antennas and applying automatic RFI flagging on SPW2. The big spikes remaining in the data are bright point sources, which should not be confused with RFI.

3.2.4 Calibration

After all the above steps, we can now begin the main calibration. The calibration was done following the basic CASA calibration flow in fig. 3.10 below,

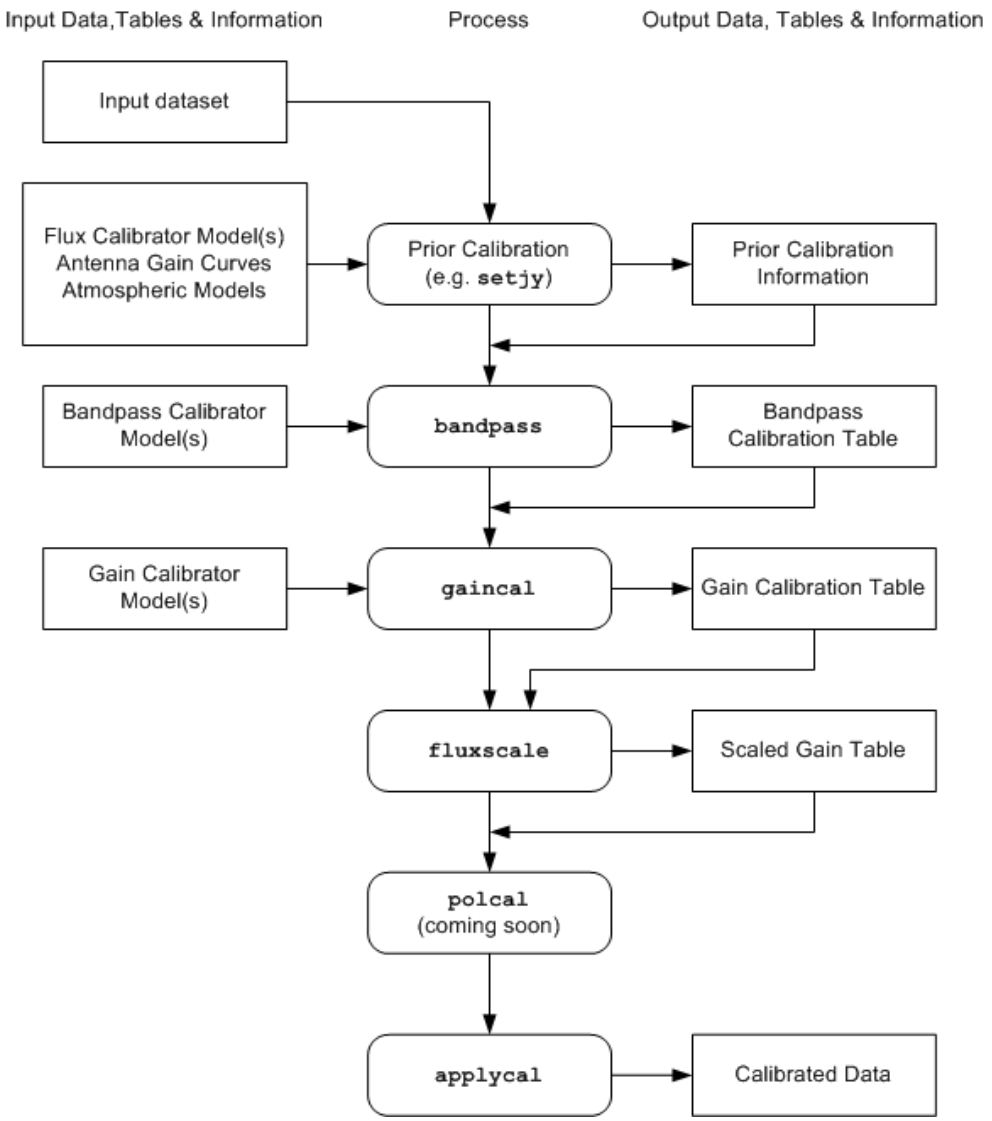

Figure 3.10: CASA calibration overflow (`https://casa.nrao.edu/docs/UserMan/casa_cookbook005.html`).

Setting Flux Density Scale

The first step of calibration is to convert the amplitudes of the observation to real astronomical units (Jy). The flux density is set by using one of the JVLA standard flux calibrators observed along with the target source. These calibrators are referred to as "primary calibrators", they are very bright sources with accurately known flux densities, usually observed at the beginning or end of observations. In our observations, **J0137+3309**, also known as

3C48, was used as the primary calibrator. 3C48 has a known spectrum and is regularly observed with the JVLA in D-configuration to determine its flux density.

Flux density scaling of the primary calibrator is performed with CASA task **setjy**. First is appropriate to add the model image of your calibrator for in case the flux calibrator is spatially resolved, and most of the time this is the case. Meanwhile our calibrator 3C48 is not resolved at L-band in D configuration, we added the model to compensate for any resolution effects if there is any. SETJY will first search for this model from model images in NRAO's model images catalog . Once the model image is added, SETJY will use specified flux density standard to compare flux measured from primary calibrator to other observed calibrators and the target sources. We used Perley-Butler 2010 standard for our calibration.

After running SETJY the following output will be shown on the logger;

Delay and Bandpass calibration

The ideal bandpass has zero phase response and a unit amplitude. Meanwhile, there are some phases and amplitude frequency dependent variation introduced to the signal at different stages of propagation. The shape of bandpass filters normally causes very steep roll-off of amplitude at the edges of each sub-band. Cables and receivers also have both amplitude and phase frequency dependent responses. The receiver itself also has a frequency dependent gain in both amplitude and phase. Bandpass calibration is an attempt to correct these frequency-dependent errors. In practice bandpass calibration is performed using a strong sources with flat-spectrum over small fractional bandwidth. The phases and amplitudes measured for flat-spectrum bandwidth will then be applied to all observations. For this work we used our primary calibrator 3C48 for bandpass calibration.

Before proceeding to bandpass calibration, delay and phase-only gain calibrations were first performed. The delay calibration is the correction of the frequency dependence slopes of the phase of incoming signal. The CASA task **gaincal** with parameter $gaintype = K$ is used for delay corrections. Phase gains calibration is done by task **gaincal** with parameter $gaintype = G$.

By applying the solutions of delay corrections and phase-only gains on-the-fly, the

CASA task **bandpass** was then used to derive bandpass amplitude and phase solutions, with the parameter *bandtype* = *B*. The solutions in fig. 3.11 were obtained.

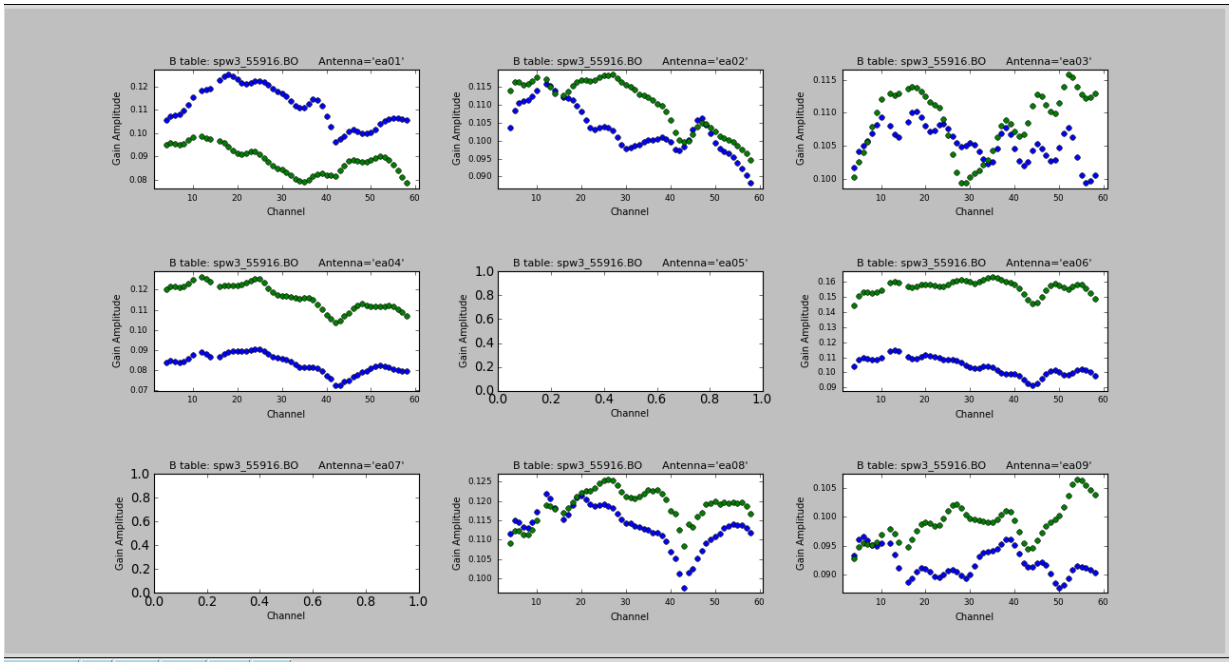

Figure 3.11: The snapshot of the bandpass amplitude solutions for different antennas. The different colours represent different polarizations. The empty boxes means that the antenna is flagged. The scale shows that bandpass have small fluctuations.

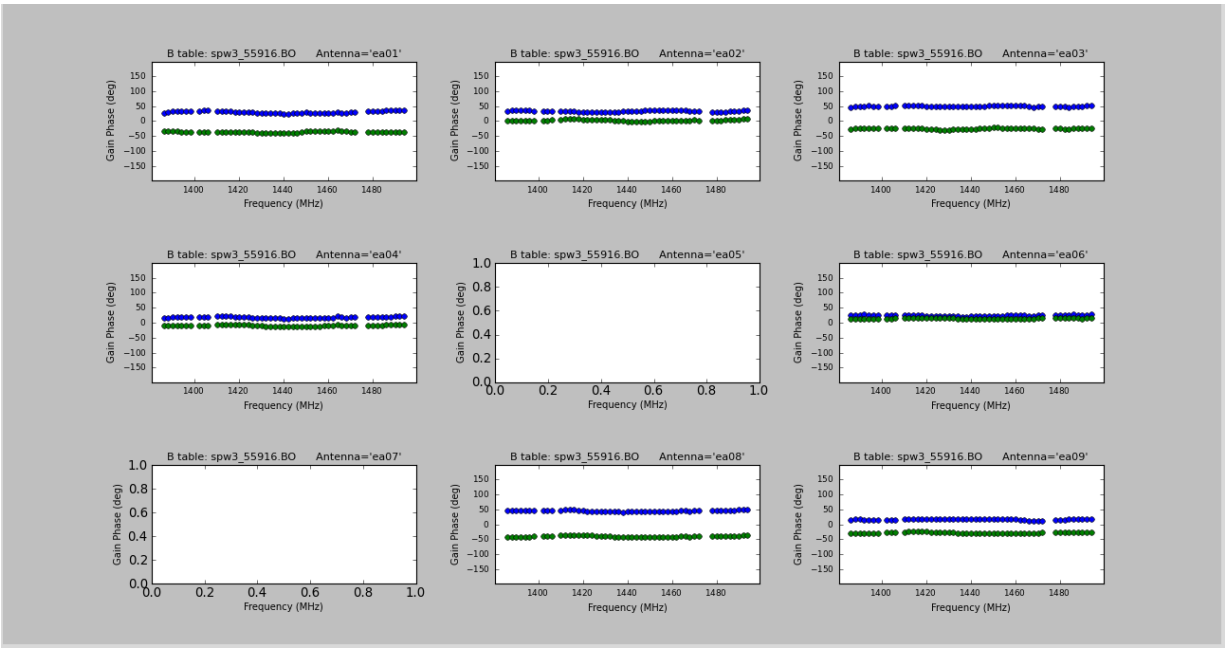

Figure 3.12: The snapshot of the bandpass phase solutions. The phase of all antennas looks good, they are constant with less than 10 % fluctuation.

Gain calibration

The next step, and the very important part of calibration is to determine the antenna-based amplitudes g_i and phase gains ϕ_i - of each antenna as a function of time from eq. (2.34). The atmosphere can cause gain fluctuations, as can instrumental effects (e.g antenna pointing error, sagging, wind loading, etc).

After solving for delay and bandpass errors, the phase for a point source is expected to be zero at the "phase centre" for every baseline. To solve for non-zero phases, along side the target source there should be a strong source observed after specific interval throughout the observation. This source is referred to as the phase calibrator. The phase calibrator should have constant amplitude and "ideal" phases of zero for all baselines throughout the observation. The measured non-zero phases are then interpolated in time and applied to the target observations.

The measured amplitudes of the phase calibrator give the measure of the system gains on each baseline. Therefore the idea is for the phase calibrator to be as close to the target

source as possible to make it possible to trace amplitudes and phase drifts brought by atmospheric changes. For this work, source **J0022+0014** was used for phase calibration.

The CASA task GAINTYPE is used for derivation of complex gains. For time-dependent gains, gaintype parameter is set to G. For this step we used another two of observed calibrators on top of the phase calibrator to retrieve all gain solutions as much as possible. The calibration was performed over a few channels free of RFI. Tables of amplitudes and phases solutions as a function of time were generated and later applied to target source. The figures below show the results of the gain calibration,

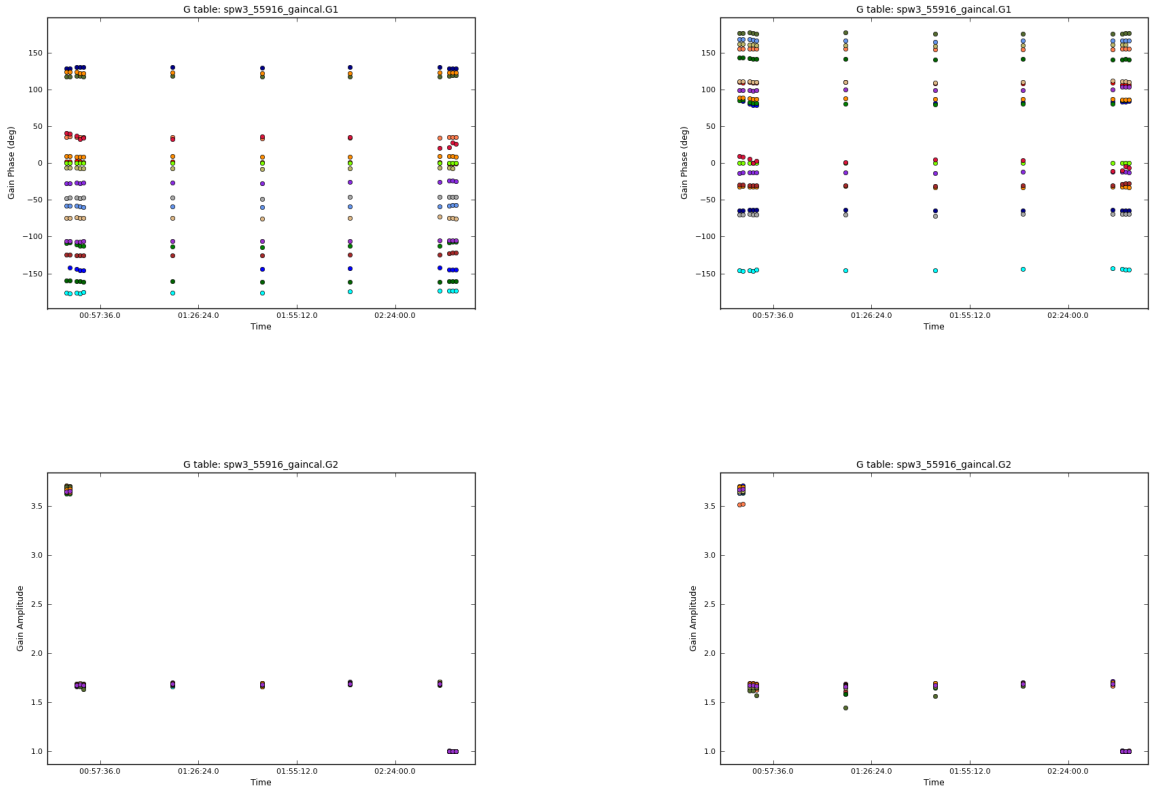

Figure 3.16: Gain amplitude solution, R polarization.

Fluxscale calibration

The final step of calibration is scale the fluxes of secondary calibrators. This task is

performed with CASA task FLUXSCALE. It does this based on the gain tables generated by the GAINCAL task. By assuming that the gain amplitude of primary and secondary calibrators is the same, the fluxes of secondary calibrators are then set with reference to the flux of primary calibrator. When running FLUXSCALE, the derived flux densities of all calibrators selected by parameter *transfer* will be printed in the logger. According to fluxes listed in `http://www.vla.nrao.edu/astro/calib/manual/csource.html`, calibrator J2253+1608 has flux of 10 Jy in L-band, which is reasonable value compared to 13.45 Jy obtained by FLUXSCALE , the phase calibrator J0022+0014, has flux density 2.70 Jy compared to 2.81 Jy obtained. These values we obtained a reasonable because the standard source flux densities are slowly variable with time.

```
Beginning fluxscale--(MSSelection version)-------
 Found reference field(s): J0137+3309
 Found transfer field(s):  J2253+1608 J0022+0014
 Flux density for J2253+1608 in SpW=0 (freq=1.378e+09 Hz) is: 13.4504 +/- 0.0105104 (SNR = 1279.72, N = 38)
 Flux density for J0022+0014 in SpW=0 (freq=1.378e+09 Hz) is: 2.81119 +/- 0.00554559 (SNR = 506.925, N = 38)
```

Figure 3.17: The snapshot of FLUXSCALE results.

Apply calibration solutions

Now that we are done with calibration, all solutions tables generated throughout calibration steps are applied to data using CASA task APPLYCAL. This task generates a corrected data column which was then split from raw data for further flagging of bad data.

Bad data flagging

After application of the calibration solutions the data were further inspected for bad data flagging. Normally after the first round of calibration the bad data missed in the first stage of flagging will clearly show up. At this stage it is safe to start flagging bad data from the target source. The second round of calibration was then performed and further bad data flagging was done.

3.3 Imaging and Self-Calibration

In this section we discuss steps followed to turn our corrected/true visibilities into sky images. Imaging was done with deconvolution algorithm “CLEAN” already discussed in

§2.3.3. In CASA, CLEAN is performed by the task CLEAN. The CLEAN task has many sub-parameters that can be changed to influence the final image. For our imaging some of the important CLEAN parameters were set as follows;

Table 3.1: CASA parameters used for imaging

CASA parameters	Used values for Imaging
mode	mfs
Imagermode	mosaic
Interactive	True
psfmode	clark
imsize	[2000,2000] (pixels)
cell	[10, 10](arcsec)
Weighting	briggs
robust	0.5
stoke	I
fftmachine	mosaic
pbcor	False

The values in the table are some of the non-default parameters found in the CASA CLEAN task. Other parameters like *weighting* and *cell* size are already discussed in §2.3. The *imsize* is the image size. Our observation is composed of many fields and separate stripes, to combine the data *mosaic* algorithm is used. The STOKE parameter is set to "I". Since we didn't perform any polarization calibration, it is important to tell CLEAN to only create the total intensity image. The parameter *mode* is set to Multi Frequency Synthesis (MFS), this is necessary for large bandwidth observations like JLVA L-band to improve UV-coverage and lower bandwidth smearing. INTERACTIVE cleaning gives the analyser opportunity check the image progress throughout the imaging process. *pbcor* is for primary beam correction.

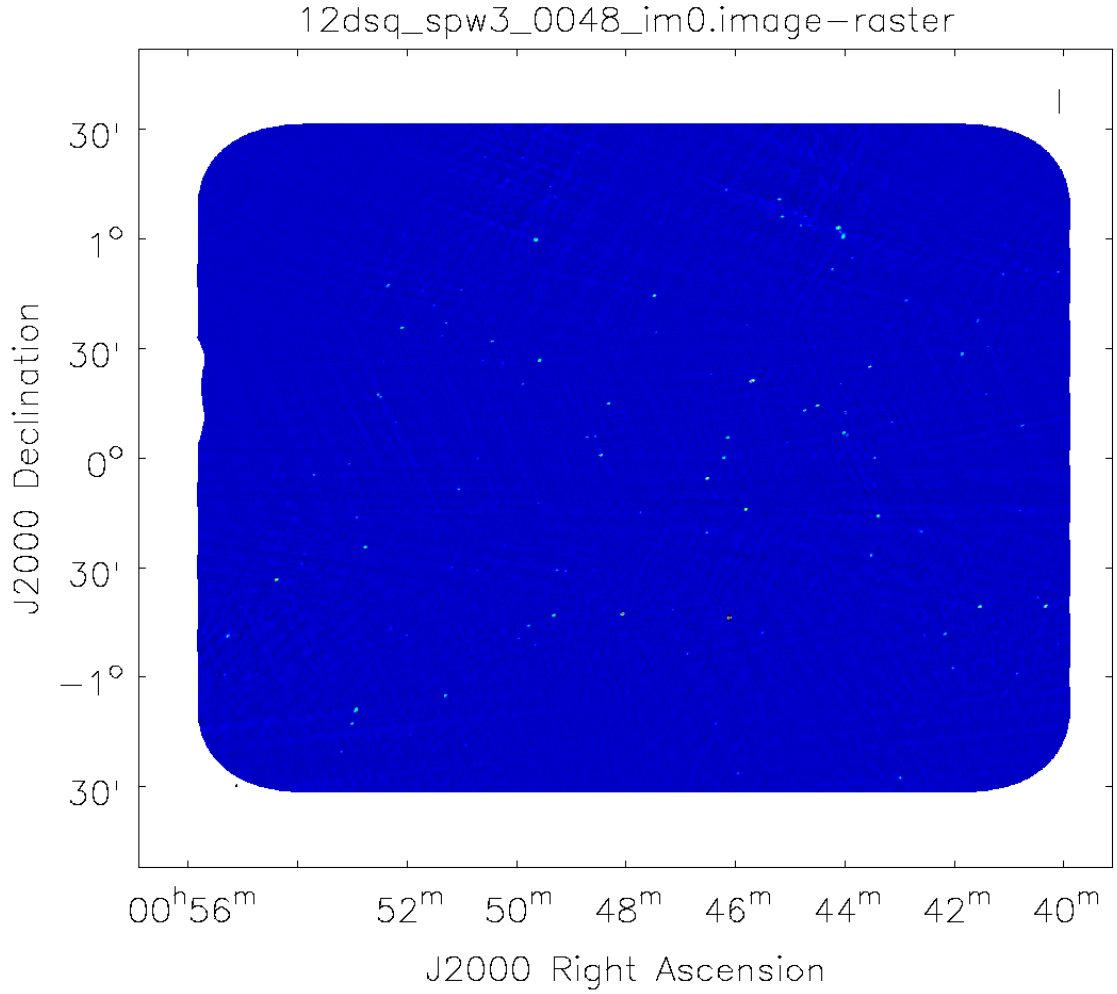

Figure 3.18: 3 deg x 4 deg patch of sky made out of SPW3 of our data. The image is already self calibrated and has an average RMS of 0.5 mJy/beam with average dynamic range of 400.

Self-calibration

The concept of self-calibration is already discussed in §2.4.2, which is needed to solve for residual amplitude and phase errors that couldn't be solved during the standard calibration process performed above. In CASA, self-calibration is performed with GAINCAL parameter, but instead of a calibrator source, we use the model created during imaging.

Our model was created in a simple way, by masking point sources while performing

CLEAN interactively. This was done with caution. Only source components which really looked like real sources were added to avoid contamination of model with fake sources. This is not the best way one can create a model, since software source finders can be recommended for finding real sources. Confusing items which looked like sources were double cross checked in The VLA's FIRST Survey catalog (**?**).

Self-calibration aims at consecutively improving this model, which in turn acts on the original data set. The CASA task GAINCAL is used for self-calibration, with *gaintype* parameter is set to G . We only performed phase calibration for self-calibration as the amplitude self-calibration turn to be complicated for continuum data. We started with interval time of 20 minutes, by setting the sub-parameter *solint*=20 minutes. After applying solutions, we cleaned again and lowered the time by 5 minutes until the artefacts on the image are reduced. The result of self-calibration are shown by fig. 4.4,

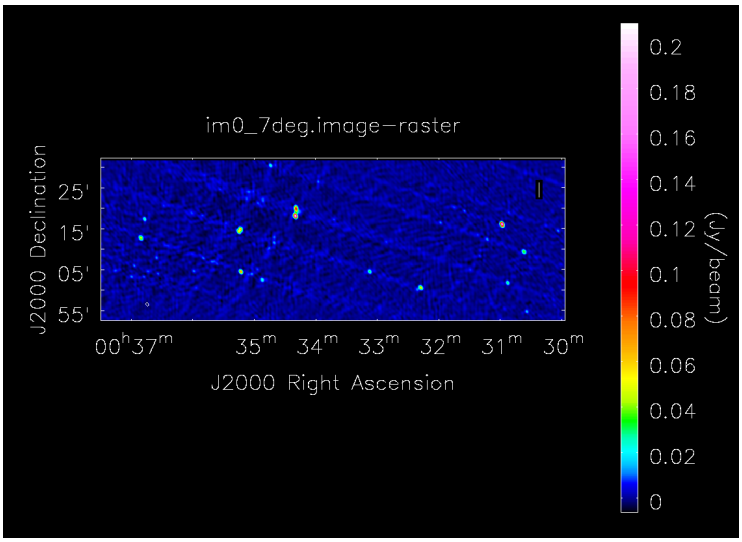

(a)

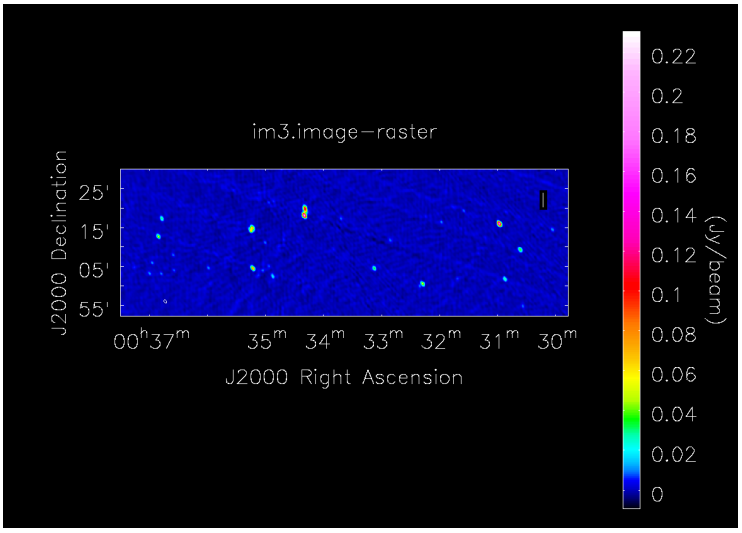

(b)

Figure 3.19: Zoomed small patch of sky before (a) and after (b) self-calibration. The image dynamic range improved from 10 to 302. Self-calibration managed to remove lot of noise in the image.

Unfortunately our data suffered from artefacts from very bright sources (>2.5 Jy/beam), mostly residing on the centre of the field. Self-calibration did not work well for these sources. An alternative way of dealing with these annoying sources will be the applica-

tion of advanced calibration techniques like peeling, which will be carried out in future work. These sources jeopardized our studies, so we ended up selecting data from regions unaffected by these sources, which will be used for cross-correlation. About half of the final map was masked. brt shows some of the annoying bright sources which could not be calibrated by self-calibration.

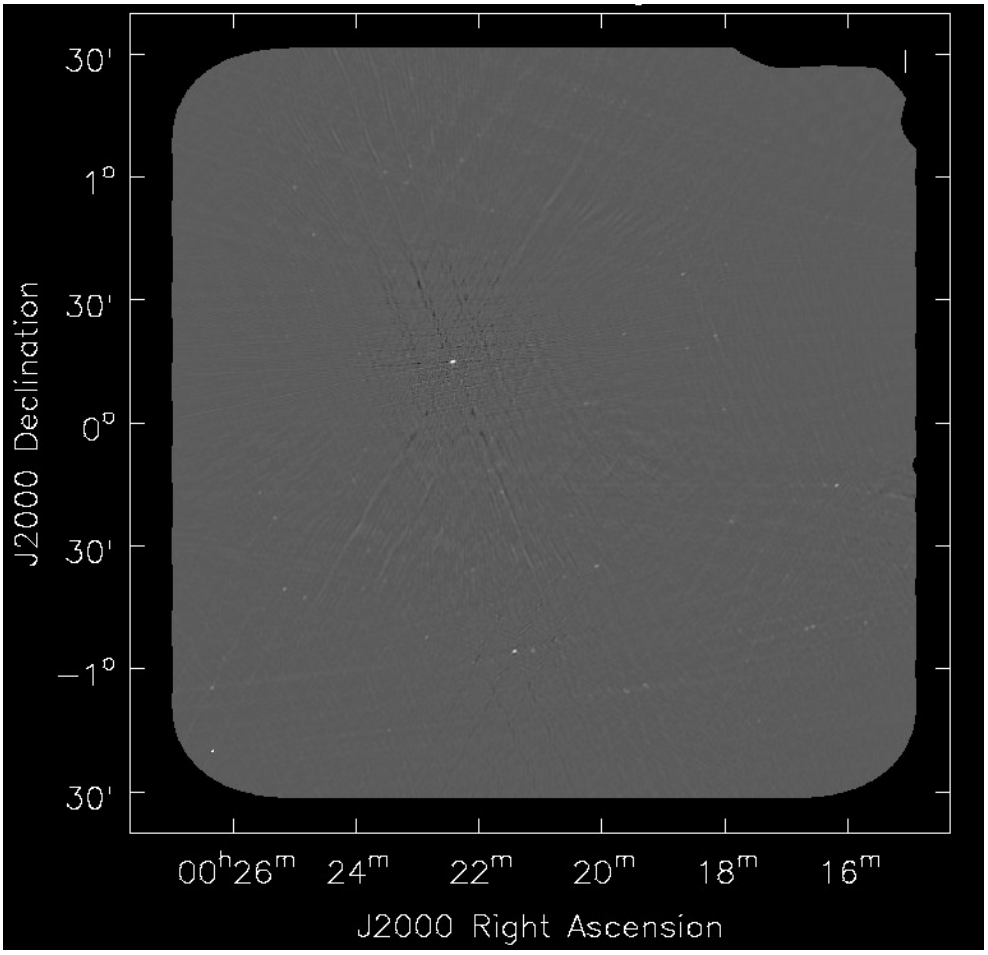

Figure 3.20: A very bright (2.0 Jy/beam) source residing at the centre of the image with sidelobes spanning almost the entire image. The brightness of the residual of this source is above 2 mJy/beam.

3.3.1 Source Subtraction

Before cross-correlation of JVLA visibilities with ACT maps, all sources brighter than 1 mJy were removed. This means that no bright AGNs are left and the majority of sources below the confusion limit of$\sim$ 89 0μJy/beam are expected to be DSFGs.

The bright sources were removed from our maps by subtracting their model visibilities generated by imaging long baseline visibilities (>2000 λ) from the whole measured visibilities. The model visibilities were subtracted from the data by using the CASA task **uvsub**. The fig. 3.21 shows the the results of source subtraction from small patch of the sky.

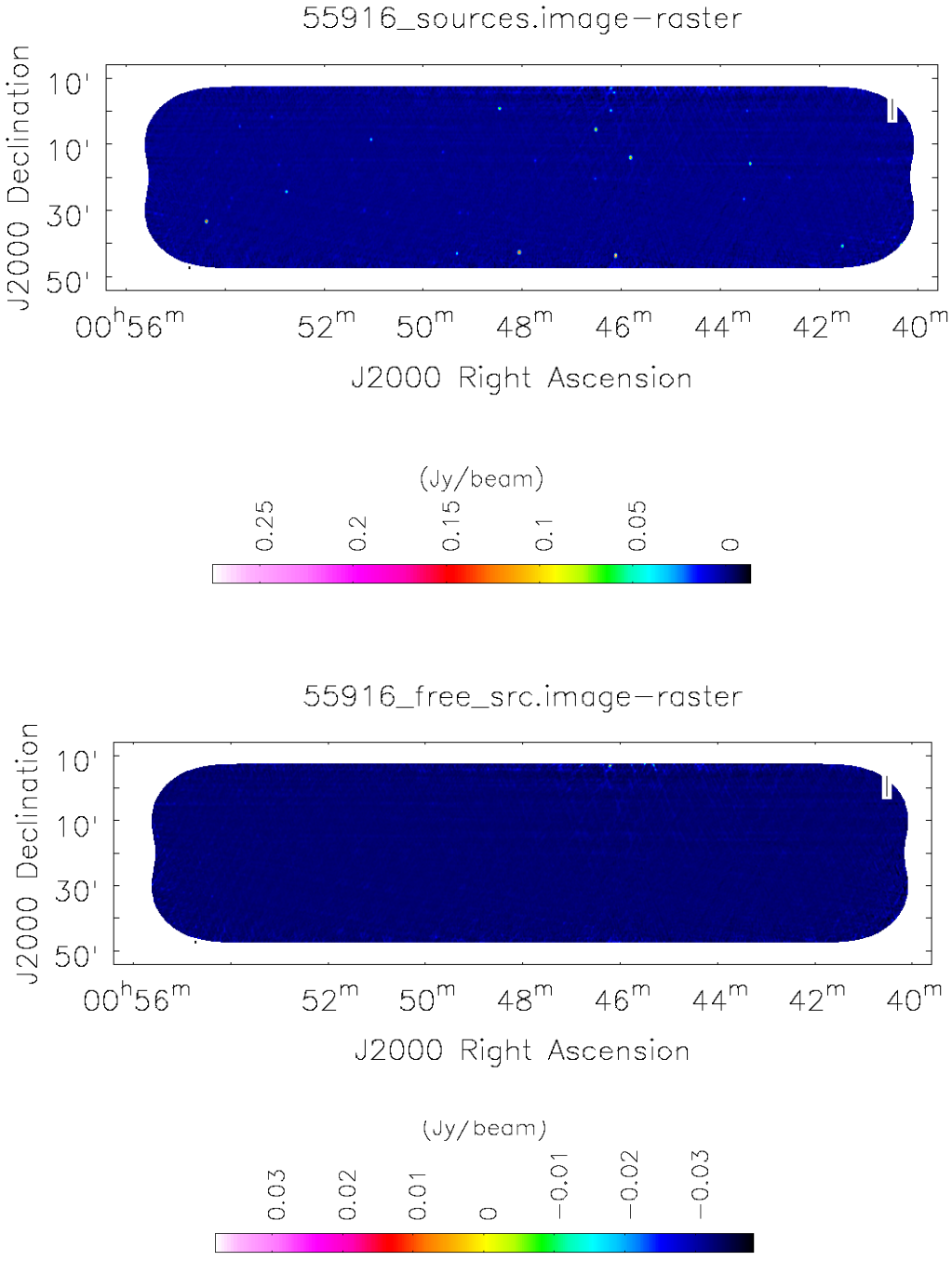

Figure 3.21: The top image shows patch of the sky before subtraction of bright sources. The bottom images shows the same patch with bright sources removed, with rms noise of 45 μJy/beam.

CHAPTER 4

Atacama Cosmology Telescope

The far-infrared data used in this study are the already processed CMB maps from the Atacama Cosmology Telescope (ACT, Swetz et al. (2011)). In this chapter, I give a brief introduction of the ACT telescope and their achievements with CMB temperature anisotropy measurements. The final section describes the process of turning ACT maps into visibilities in preparation for cross-correlation with the JVLA data. This process is done using the CASA software already introduced in chapter 3.

4.1 Description of ACT

ACT is a 6 m diameter millimetre-wavelength telescope located on Cerro Toco in the Atacama desert in northern Chile. The instrument's location, a latitude of 22.9586° South, and a longitude of 67.7875° West, makes it capable of observing about 70% of the sky in both the northern and southern hemispheres. It has an elevation of 5,190 m, which leads to excellent atmospheric transparency at millimetre and submillimeter wavelengths. Its receiver uses the Millimeter Bolometer Array Camera (MBAC), observing at frequencies

148 GHz, 218 GHz, and 277 GHz with arcminute resolution (1.4, 1.0, and 0.9) and μK sensitivity.

ACT's primary scientific goals include: 1) improving CMB anisotropy measurements by covering the small-scales, it can measure CMB temperature fluctuations from as low as multiple moments of $\ell \sim 250$ to arcminute scales of $\ell \sim$10000 (Das et al., 2014; Dunkley et al., 2013); 2) detecting and characterising the millimeter sky sources (Marsden et al., 2014); and 3) detecting massive galaxy clusters seen through their SZ signature (Menanteau et al., 2013). The choice of ACT bands enables the power separation of all these astronomical processes, the bands are also chosen to have low atmospheric opacity, and to be clear from an oxygen emission line (at 119 GHz) and water emission lines (at 183 GHz and 325 GHz).

Figure 4.1: ACT telescope in the Atacama desert in northern Chile (Swetz et al., 2011).

4.2 Observations

ACT observed two regions of the sky for four seasons, from 2007 to 2010. The first observations were done on the southern strip (ACT-S) centered around declination δ= -52.5°. The second region was an equatorial strip (ACT-E) which is $\sim$ 3° wide and spans 100°

of right ascension, centred on the celestial equator. Observed regions were selected to be away from the galactic plane to avoid contamination from diffuse galactic dust emission.

4.3 ACT CMB Power spectrum

ACT computed arcminute CMB maps and power spectrum from a total of ~ 600 deg^2 observed during 3 seasons (2008, 2009 and 2010) at 218 GHz and 248 GHz, for both the equatorial and southern strips. The first power spectra from the 2008 southern sky maps can be found in Das et al. (2011); Fowler et al. (2010), and cosmological parameters estimates were given by Dunkley et al. (2011). The final power spectrum from all combined three seasons is presented in Das et al. (2014), and Dunkley et al. (2013); Sievers et al. (2013) used it for derivation of cosmological information.

The ACT CMB power spectrum covers multipoles range of $500 < \ell < 10000$. Below $\ell \sim 3000$, where it has overlap in angular scale with several experiments, the ACT power spectrum is in good agreement with other measurements, such as from WMAP, Planck and SPT, as shown in fig. 4.2(Das et al., 2014).

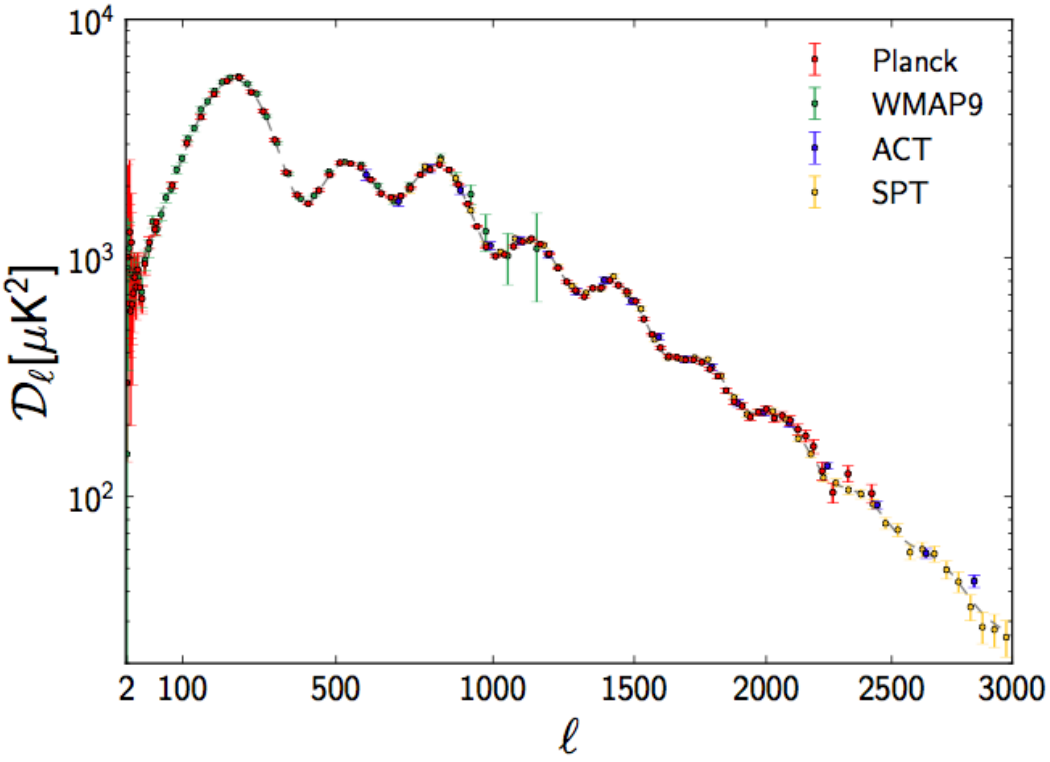

Figure 4.2: CMB temperature power spectra from combined measurements, from recent the full ACT dataset(Das et al., 2014), WMAP 9-year data release(Bennett et al., 2013), and South Pole Telescope (Story et al., 2013). The solid line is the best-fit model to ACT data merged with WMAP 7-year data (Larson et al., 2011). The dashed blue line is the primary CMB Λ CDM model including lensing. ACT and SPT spectra start from $\ell \sim 450$ to 3000.

4.4 ACT CMB Foregrounds

Above $\ell \sim 1500$, the power of primary CMB anisotropies drops exponentially and foregrounds power start dominating and continue growing with ℓ as shown in fig. 4.3. ACT foregrounds composed of radio sources (AGNs), Infrared sources (DSFGs), and secondary anisotropies from both kinetic-SZ and thermal-SZ.

The total power measured by ACT can be represented by the equation,

$$D_\ell^{sky} = D_\ell^{CMB} + D_\ell^{forg}, \tag{4.1}$$

where,

$$D_\ell = \frac{\ell(\ell+1)C_\ell}{2\pi} \tag{4.2}$$

.

D_ℓ^{CMB} is the power of the lensed primary CMB power spectrum and D_ℓ^{forg} is the power spectrum of foregrounds. Foregrounds power can be further be separated into different components as follows:

$$D_\ell^{forg} = C_\ell^{Gal} + C_\ell^{CIB} + C_\ell^{radio} + C_\ell^{tsz} + C_\ell^{ksz} \tag{4.3}$$

where C_ℓ^{Gal} is diffuse galactic components, mainly galactic dust. Even though ACT observations are conducted in regions of low galactic dust, there is detectable galactic dust power especially on ACT -E region, which can be modelled using the (Finkbeiner et al., 1999) map and recent released Planck's maps (Planck Collaboration et al., 2015) .

Other diffuse foregrounds, synchrotron and free-free foregrounds, are negligible at ACT observing frequencies. C_ℓ^{CIB} is the CIB power from DSFGs, C_ℓ^{radio} is the radio source power component and C_ℓ^{tsz} and C_ℓ^{ksz} are the power from thermal and kinetic SZ. fig. 4.3 shows the power of these different components after removal of the galactic dust component at 148 GHz.

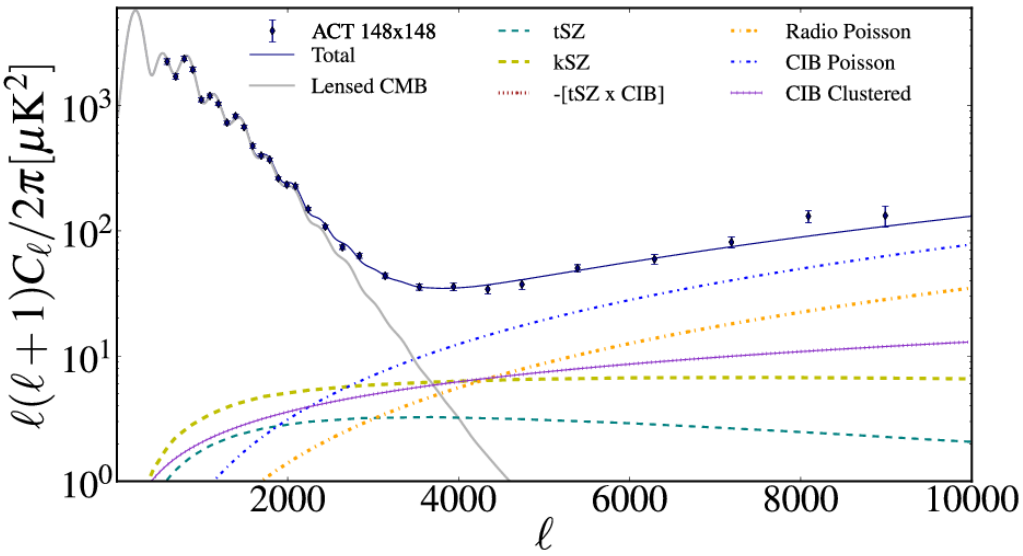

Figure 4.3: 148 GHz ACT power spectra and best-fit model obtained from (Dunkley et al., 2013), with best-fit contributions from the SZ effect, Poisson and clustered Radio and Infrared source foregrounds.

4.4.1 Radio sources

From the catalogue presented by Marsden et al. (2014), 167 of 198 extragalactic sources detected by ACT at 148 GHz and 218 GHz are reported to be radio galaxies powered by AGN. Their spectrum is consistent with synchrotron emission with typical spectral indices of α_s=-0.5 (Marriage et al., 2011). Most of the AGN power can be removed from ACT maps by masking them to a threshold of 15 mJy. The residual power from radio galaxies lying below the threshold at ℓ=3000 is reported to be $a_{(s)}$=2.9 $\pm$ 0.4 μK^2 (Sievers et al., 2013).

From assumptions made by Hall et al. (2010) at 150 GHz, only the Poisson power term of radio galaxies needs to be considered at ACT frequencies and the clustering term is negligible, with an expected power of only 0.001μ K^2.

4.4.2 DSFGs

The ACT-detected DSFGs have a median spectral index of, $\alpha_{148-218} = 3.7^{+0.62}_{-0.86}$ spanning from local redshifts to redshifts around 6. Their SED follows the modified blackbody spectrum $S_v \propto v^{\beta} B(v, T_{eff})$. Most of the DSFGs detected by ACT have counterparts from existing deep catalogues from the Infrared Astronomical Satellite (IRAS (Helou et al., 1988)) and SPT (Vieira et al., 2010). Those with no counterparts are believed to belong to a gravitationally lensed population of DSFGs. Detailed report on DSFGs detected by ACT is given in (Marsden et al., 2014; Marriage et al., 2011).

The contribution of DSFGs to Cosmic Infrared Background has been already discussed in previous chapters. Both Poisson and clustered power from DSFGs are expected to contribute significantly to the ACT power spectrum. The power from DSFGs can now be written as,

$$D_{\ell}^{CIB} = D_{\ell}^{CIB-Poisson} + D_{\ell}^{CIB-Clustered} \tag{4.4}$$

where D_{ℓ}^{CIB-P} represents the Poisson term, and D_{ℓ}^{CIB-C} represents the clustered term.

After bright DSFGs the residual clustering and Poisson power is constrained to be a_c=5.0 $\pm$ 1.0 μK^2 and a_p=7.0 $\pm$ 0.5 μK^2 respectively at ℓ=3000 (Sievers et al., 2013).

4.4.3 Sunyaev-Zeldovich effects

The interaction of CMB photons with the intra-cluster medium (ICM) results in a small distortion of the CMB radiation, in an effect known as the Sunyaev-Zeldovich effect (SZ). If the intensity change is caused inverse Compton scattering of CMB photons by hot electrons in the ICM, the effect is referred to as the thermal SZ (tSZ) effect (Sunyaev & Zeldovich, 1970). The effect can also result from the Doppler effect caused by a peculiar motion of gas with respect to the CMB rest frame, known as the kinematic SZ (kSZ). More detailed information about ACT's SZ measurements can be found in Hill et al. (2014); Hasselfield et al. (2013).

4.5 Preparation of ACT Maps

This work uses CMB maps from ACT season 4 equatorial observations available from `http://lambda.gsfc.nasa.gov/product/act/act_maps2013_get.cfm`. The maps used are bright point sources free and the only signal expected on them is believed to come from the CMB and some residual foregrounds, especially the DSFGs signal. Figure 4.4 shows the extracted CMB map patch that we used for this work. This patch overlaps with our JVLA maps. The map was first tapered to remove noise on the edges before we use it.

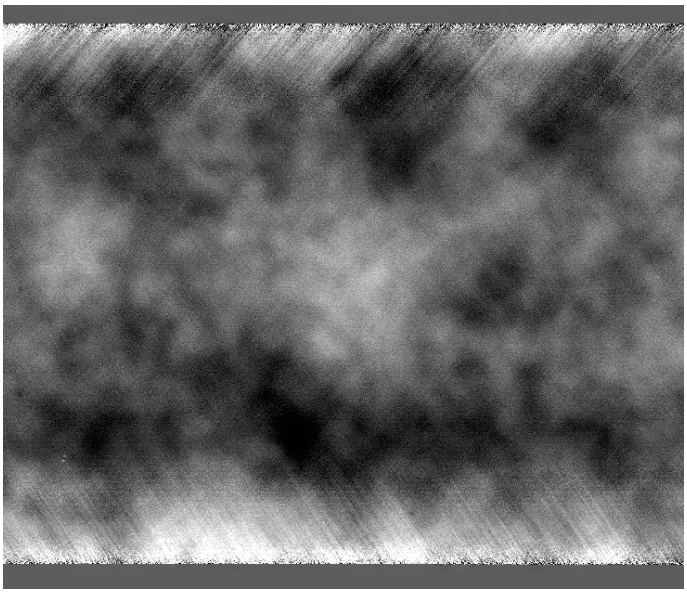

(a)

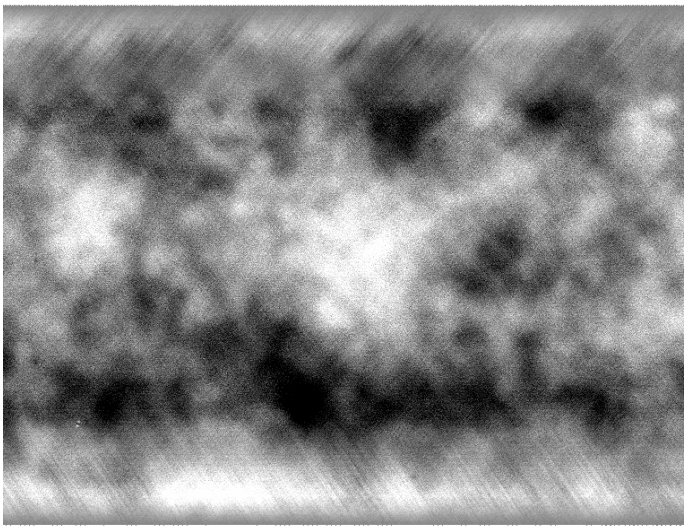

(b)

Figure 4.4: A patch extracted from ACT season 4 equatorial CMB map. 4.4(a) shows the original patch extracted with noisy edges. 4.4(b) shows the same patch after tapering the noise on the edges.

The far-infrared radio correlation will be performed in the UV domain. To compare two

observations in the UV domain, both observations should have the same UV coordinates. To make this possible, we take our ACT CMB sky model and predict the model visibilities that would be seen by the JVLA. In this case, the data will be predicted for all coordinates available in the MS file. First, the sky model was modified for CASA to be able to read it. The header of the model must have 4-dimensional WCS, two spatial coordinates, a FREQUENCY axis, and a STOKES axis otherwise the CASA will show an error when used without these axes. The CASA importfits() task and **simutil()** module were used to perform this process. Importfits reads the fits file into an image, and Simutil gives options to update the centre observing frequency and bandwidth of observation. These parameters can be acquired from the logger when running **listobs()**.

Once our model was read into CASA, model visibilities were predicted using the simulator tool-kit which is inserted in CASA as "sm". First, the telescope used for the observation was specified, the command *setvp*() sets the primary beam of the telescope (done using the telescope's name), and finally run *sm.predict* to predict visibilities. In fig. 4.5 we show a small patch of image from predicted visibilities, this image now has the JLVA spatial filter applied to it, should not look like the original ACT image.

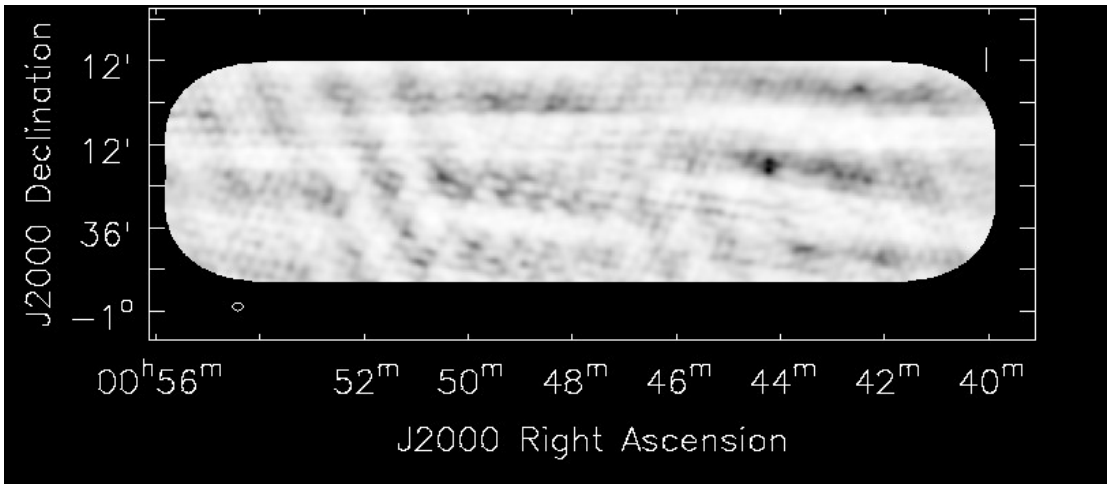

Figure 4.5: Small patch imaged from simulated visibilities.

CHAPTER 5

Radio-Far Infrared correlation

5.1 Introduction

The non-thermal synchrotron emission from a wide range of galaxy types is observed to form a tight correlation with the FIR emission which holds over 5 orders of magnitudes in luminosity. This correlation is termed the Radio-Far Infrared (R-FIR) correlation (Condon, 1992; Yun et al., 2001; Helou et al., 1985; van der Kruit, 1971). There is still no solid explanation of why the emissions from different origin mechanisms can be tightly correlated like that. Currently the existing theoretical explanation is that is driven by star formation activities. The cosmic-ray electrons responsible for synchrotron emission are accelerated to relativistic speeds by shock waves of supernovae (SNe) explosions of newly born massive stars ($M > 8M_{\odot}$). The rate of supernova explosions is expected to increase with increasing star formation, hence non-thermal emission from star forming regions is a good tracer of SFR. On the other hand, the UV light from the same young stars responsible for supernovas is absorbed by dust particles within star forming regions, which then re-emit at FIR wavelengths of about 60-200 μm, therefore FIR luminosity is also good tracer of

SFR (Condon, 1992).

The R-FIR is mostly studied by measurement of the q-value, the ratio between radio and FIR flux densities;

$$q = log(\frac{S_{FIR}}{3.75 \times 10^{12}(Wm^{-2})}) - log(\frac{S_{1.4GHz}}{(Wm^{-2}Hz^{-1})}) \tag{5.1}$$

The quantity S_{IR} is the integrated flux density between 42.2-122.5 μm, and 3.75×10^{12} is the mid frequency of the band, $S_{1.4GHz}$ is the observed flux density of radio emission at 1.4 GHz.

5.2 Evolution of R-FIR correlation with the Redshift

The subject of the evolution of the R-FIR with redshift is very important for the current study as we depend on the R-FIR to measure the signal of galaxies residing at higher redshifts. The local galaxies have been shown to strongly obey the F-FIR at all local redshifts (Condon, 1992; Helou et al., 1985), with an average q value of 2.34. Currently there is no clear evidence of evolution of the correlation with the redshifts, however, there are some reasons that may lead to the collapse of the correlation at higher redshifts. For example, the interaction of electrons with the CMB radiation (energy density of which scales as $(1+z)^4$) results in diminishing radio emission at high-z (Murphy, 2009; Schleicher et al., 2013). The higher-z galaxies are also considered to be more luminous hence have high flux densities, which leads to a change in the q value.

Several studies reported an offset in the correlation at higher-z (Ivison et al., 2010; Magnelli et al., 2010). (Magnelli et al., 2010) measured average q value to be 2.17 for some of the SMGs at higher-z, this value is lower than the one reported for local galaxies. Ivison et al. (2010) argued that q $\propto (1+z)^{\alpha-1}$, where α is a radio spectral index, therefore a slight change in the radio spectral index can affect the value of q for high-z galaxies. The value of α is assumed to be -0.8 for local star-forming galaxies (Condon, 1992), but some authors reported the value to range between -0.6 and -0.7 (Garn & Alexander, 2008).

To look more at the evolution of R-FIR correlation with redshift, the recent study by Schober et al. (2016) investigated this matter in more details. In their study, they theoretically studied how R-FIR span from lower-z to higher-z by using models of the galaxy at z=0 and a starburst at z=2.6. They derived radio luminosity as a function of redshift and show that the radio luminosity decreases towards higher-z due to increasing cosmic ray energy losses at high-z, which results in the decrease of the q value. The fig. 5.1 represents the results for their two models. The model at z=0 is in good agreement with the observational data from Yun et al. (2001), represented by the grey points. When they increase the redshift, the ratio of FIR and radio luminosities start to decrease hence decreasing q. These results are in agreement with Murphy (2009), who studied the R-FIR correlation of sub-mm galaxies up to z=2.6.

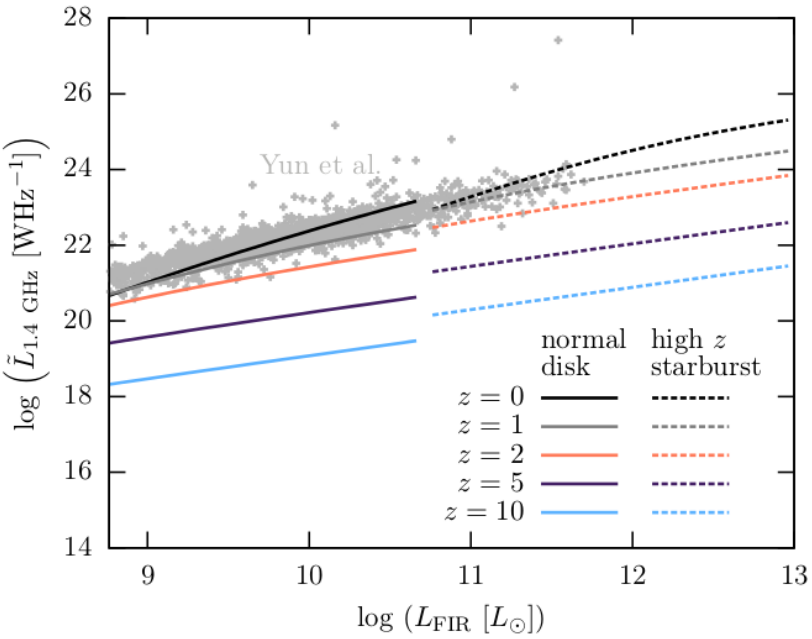

Figure 5.1: The radio luminosity L_{radio} as a function of Infrared luminosity L_{RIF} for different sets of redshifts. The calculated R-FIR correlation from the model at z=0 (shown by the orange line) lie nicely on top of observational data from Yun et al. (2001). The dashed lines with different colours correspond different redshifts, it can be seen that the ratio of radio to infrared luminosity decreases with increasing redshift.

5.3 The R-FIR correlation in the current study

This study is based on the R-FIR to measure the clustering component of DSFGs in the ACT maps. From the radio source counts discussed in fig. 1.5, the 1.4 GHz radio surveys are dominated by AGN's above 1 mJy flux, while fluxes below that are dominated mainly by DSFGs and some radio quit AGN's. After removing bright AGN's, the confusion-limited radio map will be left with faint AGNs and DSFGs. This means that the correlation between deep 1.4 GHz continuum data with bright sources removed and the CMB data will be able to detect the signal from the DSFGs.

This study will also tell us more about the redshift distribution of the DSFGs. Radio observations has been used as one of the tools to study sub-mm sources, which are hardly visible at optical wavelengths because of dust obscuration. This makes it hard to determine their redshifts, but JVLA observations can provide their true optical counterpart. Depending on the R-FIR correlation, the redshifts can be estimated from the spectral index from radio to sub-mm fluxes (Carilli & Yun, 2000; Miller & Owen, 2001). Therefore the final results of this study can tell us more about the redshifts of the DSFGs as the amplitude power spectrum of intensity variations as function of the angular scales gives details on the redshift distribution of galaxies.

5.4 R-FIR correlation estimation method

The R-FIR correlation can be obtained by different methods, for example, the q-ratio method (Yun et al., 2001; Helou et al., 1985) and wavelet multi-scale (Frick et al., 2001). In this work we use the covariance matrix estimation,

$$C(v_i, v_j) = \frac{1}{N} \sum_{k=1}^{N} (V_i^k - \bar{V}_i)(V_j^k - \bar{V}_j)^* \tag{5.2}$$

The term $V_i(u, v)$ represents visibilities of the JVLA observation, while $V_j(u, v)$ represents the visibilities mocked from ACT CMB maps, N is number of visibilities in a bin, $*$ is complex conjugate operation, and $\bar{V}_i$ is the average visibility in each bin. In principle the

$\bar{V_i}$ should be zero for clean data. To avoid noise bias on the correlation, both data sets were divided into N_{sub} independent bins of width $\triangle$UV=50λ, the noise is then expected to be roughy constant in each bin. The covariance matrices were then estimated for each bin using eq. (5.2), with N now representing the number of independent realisations in the independent bins. We measure the complex correlation between ACT and JVLA. We expect this correlation to be strictly real, so the imaginary term is an independent estimate of the noise.

The uncertainty of the covariance matrix was estimated from the scatter of covariance between JVLA visibilities and the visibilities mocked from ACT maps that have been shifted to get rid of any astronomical signal. The covariance matrix was then calculated between the bins of actual JVLA visibilities and new shifted ACT visibilities. This means that no correlation is expected between $V_i(u,v)$ and the new $V_j(u,v)$, so the covariance matrix will just represent the noise. The covariance was calculated for 10 sets of shifted model visibilities.

5.4.1 Results

5.4.1.1 Clustered DSFGs Power

First, we present the power spectrum of cross-correlation between the simulated CMB map and JVLA to demonstrate the expectations of ACT cross JVLA expectations. The simulated CMB map is fitted with the dusty galaxies signal modeled by some of the Poisson and clustered components from Dunkley et al. (2013) estimated by

$$C_{CIB} = a_p(\frac{\ell}{\ell_0})^2 + a_c(\frac{\ell}{\ell_0})^{2-n} \tag{5.3}$$

where C_{CIB} is the total power, a_p and a_c are parameters describing the Poisson power and clustering power respectively, n is a power law index estimated to be 1.2, therefore the clustered component scale as $\ell^{0.8}$. The power is normalised at ℓ_0=3000 and 150 GHz.

The fig. 5.2 shows the results of the correlation of our simulated CMB maps and JVLA. The top panels is the clustered dusty galaxies signal with model fit and the bottom panel

is the Poisson signal component.

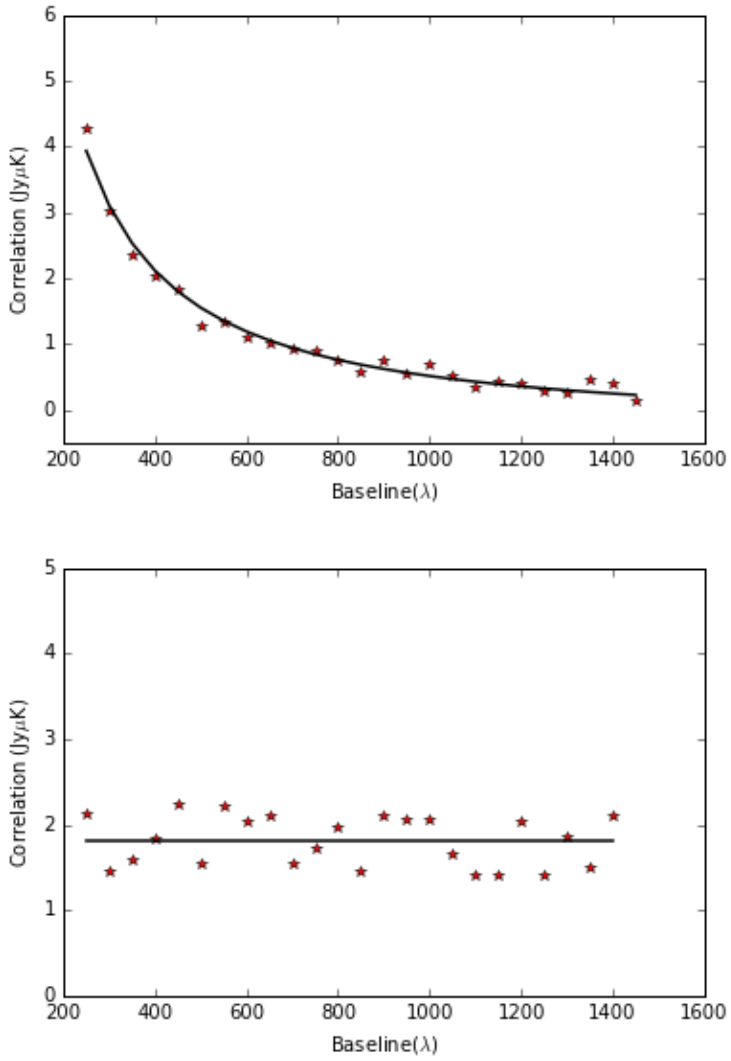

Figure 5.2: The simulated CMB-JVLA cross spectrum for the clustered (top) and Poisson (bottom) terms from the templates from Dunkley et al. (2013), and assuming a radio/far-infrared flux ratio of 1. The amplitude of the observed cross-correlation relative to these templates tells us the measured value of the radio far-infrared ratio.

The power spectrum of the cross-correlation between ACT and JVLA was performed only from 10 deg^2 patch of the sky from both SPW3 and SPW6 of our JVLA data due to RFI contamination and the bright source effects we had on the data as already mentioned.

The power is computed for both 148GHz and 220 GHz ACT maps. The table 5.1 is the average correlation power from SPW3 and SPW6. The *Real* and $Imag$ represents the real part and imaginary part of the cross-correlation power respectively.

The mean correlation was calculated using the equation,

$$C_{mean} = \frac{1}{1/\sigma_1^2 + 1/\sigma_2^2}(\frac{C_{spw3}}{\sigma_1^2} + \frac{C_{spw6}}{\sigma_2^2}) \tag{5.4}$$

where C_{spw3} is the correlation from SPW3, C_{spw6} is the correlation from SPW6 and σ_1 and σ_2 is their respective errors. The error of the mean correlation was then obtained by

$$\sigma_{mean}^2 = \frac{1}{1/\sigma_1^2 + 1/\sigma_2^2}. \tag{5.5}$$

The fig. 5.3 shows the mean cross-correlations power of Poisson and clustered signal from both 148GHz and 220GHz frequencies over-plotted in the same graph. There is a high power seen at short baselines between 250 to 400λ for both frequencies with 220 GHz having stronger power spectrum than 150 GHz as expected from dusty galaxies. The correlation is also consistent with the correlation power from simulated and JVLA as shown by fig. 5.2. The power scale down when moving towards large scales as expected for clustered component of dusty galaxies. These results are also are in agreement with other studies González-Nuevo et al. (2005); Hajian et al. (2012); Lagache et al. (2007); Thacker et al. (2013); Amblard et al. (2011) which reports the increase of clustering signal of DSFGs towards smaller angular scales.

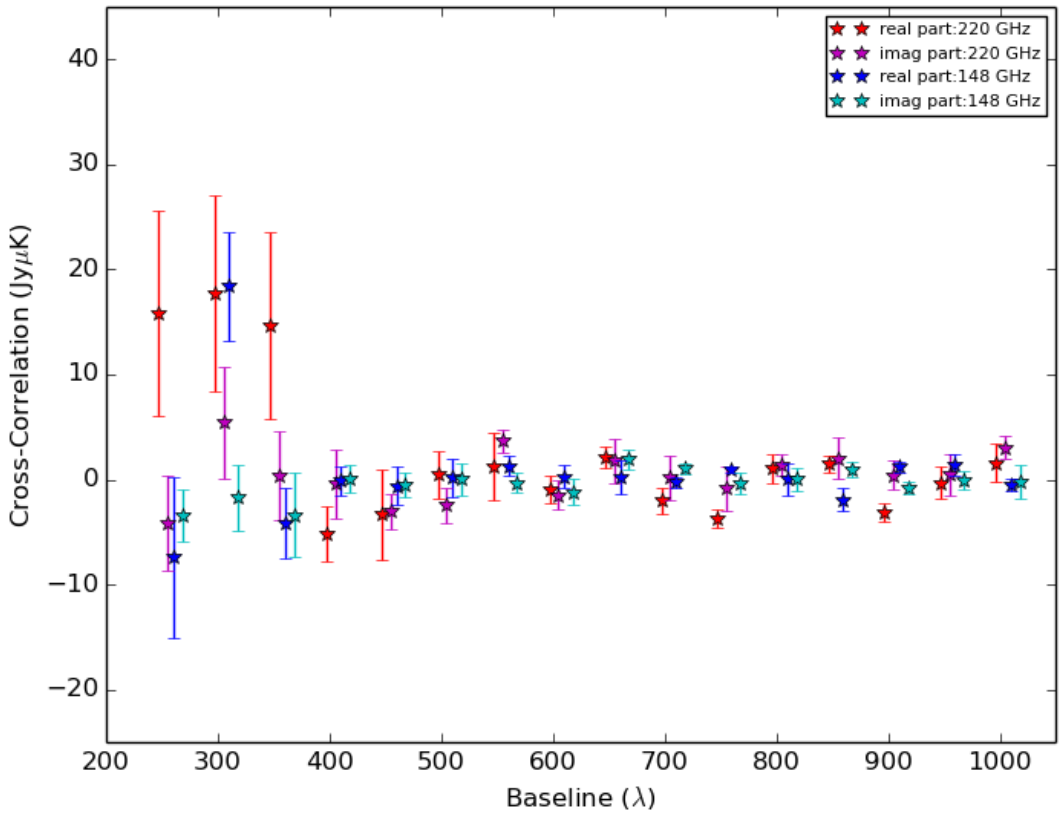

Figure 5.3: The correlation power versus the baseline from both 148 GHz and 220 GHz ACT map cross JVLA over plotted together. The blue and red points represent the points from real parts of correlation from 148 GHz and 220 GHz frequencies respectively. Cyan and magenta colors represent the imaginary parts of the correlation from 148 GHz and 220 GHz frequencies respectively. The data points are slightly shifted by 5λ to the right for clarification. There is high signal seen at short baselines signifying clustered component of dusty galaxies. The 220 GHz show to have stronger signal than 148 GHz as expected to be for clustered dusty galaxies.

5.4.1.2 Redshift Distribution

We also estimate the mean clustered DSFGs redshift from our cross-correlation. The redshift distribution is estimated from fitting the model of DSFGs to our data and compared

the results to the R-FIR spectral energy density (SED) of submillimeter galaxies from Michałowski et al. (2010). The top panel of fig. 5.4 shows the ACT 220 GHz , JVLA power spectrum with the best fit of Poisson and clustered model. The bottom panel shows the radio-FIR ratio of the clustered component as measured from our data compared against the expected ratio as a function of source redshift. The solid red line shows our measured value of 2.12 ± 0.41. We find the measured correlation is consistent with the low redshift for the clustered sources. We see no evidence for Poisson component of correlation as would be expected for higher redshift origin of these sources.

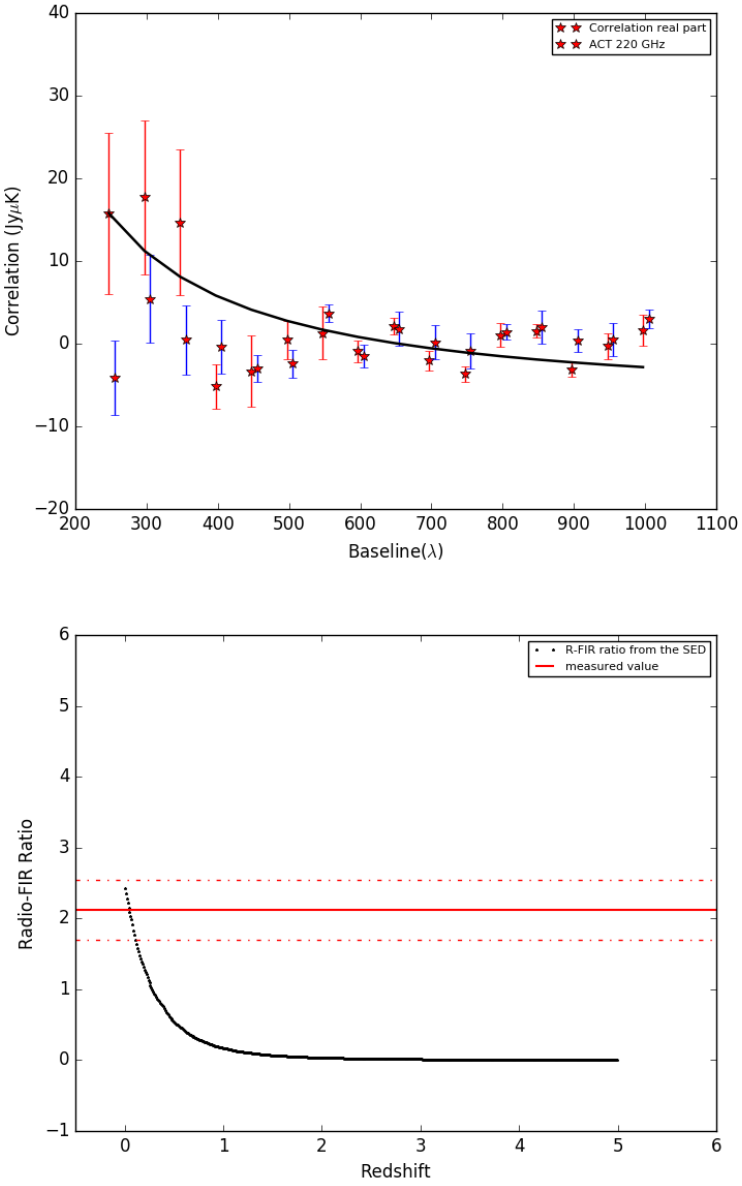

Figure 5.4: The top panel is the ACT's 220 GHz cross JVLA power spectrum with best fit of both Poisson and Clustered terms. The best fit is shown by the by black line. Bottom panel: Black curve shows the expected R-FIR ratio as a function of redshift as predicted by SED of Michałowski et al. (2010). Red line shows our measured value and 1σ error. Our data prefer a very low redshift (z<0.5) of the clustered DSFGs.

Table 5.1: The power spectrum cross-correlation between ACT and JVLA.

	Mean cross-correlation (148 GHz) [JyμK]				Mean cross-correlation (218 GHz) [JyμK]]			
Baseline [λ]	Real	ΔReal	Imag	ΔImag	Real	ΔReal	Imag	ΔImag
200-250	-7.38	7.64	-3.35	2.485	15.8	7.64	-4.11	2.48
250-300	18.4	5.18	-1.73	3.09	17.7	5.18	5.42	3.09
300-350	-4.12	3.35	-3.37	3.97	14.7	3.35	0.44	3.97
350-400	-0.10	1.15	0.09	1.27	-5.21	1.42	-0.41	1.27
400-450	-0.58	1.88	-0.45	1.16	-3.33	1.88	-3.03	1.16
450-500	0.22	1.82	0.06	1.52	0.44	1.82	-2.43	1.52
500-550	1.29	0.96	-0.30	0.97	1.29	0.96	3.68	1.00
550-600	0.28	1.09	-1.16	1.19	-0.92	1.09	-1.50	1.19
600-650	0.21	1.65	1.93	0.94	2.13	1.65	1.80	0.94
650-700	-0.28	0.53	1.09	0.52	-2.02	0.53	0.18	0.52
700-750	0.91	0.31	-0.30	1.03	-3.68	0.31	-0.86	1.02
750-800	0.05	1.51	0.05	1.11	1.04	1.51	1.42	1.11
800-850	0.03	1.11	0.94	0.74	1.52	1.11	2.01	0.74
850-900	-1.94	0.52	-0.73	0.58	-3.08	0.52	0.41	0.58
900-950	1.38	1.02	-0.01	0.90	-0.31	1.02	0.46	0.90
950-1000	-0.44	0.57	-0.19	1.60	1.61	0.57	3.02	1.60

CHAPTER 6

Conclusions and Future Work

This chapter provides additional ideas for future work to improve the results of this study, as well as conclusions.

6.1 JVLA Data analysis

We have presented the data analysis of JVLA On-The-Fly (OTF) scan observations. The OTF scans have proven to be promising for future large sky surveys from instruments like SKA and MeerKAT. We have calibrated and imaged 3 spectral windows out of 8 total in the data. These SPWs were chosen because of lower RFI contamination. Our images have mean rms noise of 50 μJy/beam. This is comparable to the approximate confusion limit of 89 μJy/beam. We have found that self-calibration is not working well near bright sources, this might be due to short observing periods of any given field, as the field only remains within the primary beam for five seconds.

The future data analysis work will be to remove RFI from other promising SPW's. Automatic RFI removal has proven to perform a good job on SPW2 which had more RFI

than SPW3 and SPW6. We will also apply advanced time-dependent calibration to remove the effects of bright sources from our data, hence utilise all the data for the cross-correlation.

6.2 Cross-correlation

We have also presented the cross-correlation power spectra between JVLA radio observations and 148 GHz and 220 GHz ACT CMB maps. While no firm conclusion can be drawn from these results, the results are consistent with the expectations from clustered dusty galaxies power component as shown by the correlation from simulated data and other studies. The results also show the presence of signal at short baselines but not on long baselines as expected for the clustered component for dusty galaxies. We find a significant detection in the ACT 220 GHz cross JVLA, but a marginal one at 148 GHz. This is consistent with a dusty galaxy spectrum in ACT as expected from the R-FIR correlation. We also estimate the redshift ($z< 0.5$) of the measured signal corresponding to a low-redshift origin of the clustered component of dusty galaxies.

Future work will involve performing cross-correlation with more radio data. We also would like to perform the cross-correlation with other infrared/sub-mm data which overlap with our observation, for example, *Herschel* surveyed this field and radio observations from the MeerKAT telescope will clarify the findings of this study. With more short baselines, MeerKAT will be better suited to this work than JVLA. We will propose get MeerKAT data to continue this work with more sensitivity.

Bibliography

Michałowski, M., Hjorth, J., & Watson, D. 2010, ApJ, 514, A67

Aghanim, N., Majumdar, S., & Silk, J. 2008, Reports topic definitionon Progress in Physics, 71, 066902

Hill, J. C., Sherwin, B. D., Smith, K. M., et al. 2014, arXiv:1411.8004

Hasselfield, M., Hilton, M., Marriage, T. A., et al. 2013, JCAP, 7, 008

Barger, A. J., Cowie, L. L., Sanders, D. B., et al. 1998, Nature, 394, 248

Bennett, C. L., Hill, R. S., Hinshaw, G., et al. 2003, ApJS, 148, 97

Hinshaw, G., Larson, D., Komatsu, E., et al. 2013, ApJS, 208, 19

Abazajian, K. N., Arnold, K., Austermann, J., et al. 2015, Astroparticle Physics, 63, 66

Hu, W., & White, M. 1997, ApJ, 479, 568

Brandt, W. N., Lawrence, C. R., Readhead, A. C. S., Pakianathan, J. N., & Fiola, T. M. 1994, ApJ, 424, 1

Frick, P., Beck, R., Berkhuijsen, E. M., & Patrickeyev, I. 2001, MNRAS, 327, 1145

Schober, J., Schleicher, D. R. G., & Klessen, R. S. 2016, arXiv:1603.0269

Blain, A. W., Smail, I., Ivison, R. J., Kneib, J.-P., & Frayer, D. T. 2002, Physics Reports, 369, 111

Blain, A. W., Barnard, V. E., & Chapman, S. C. 2003, MNRAS, 338, 733

Blanchard, A., & Schneider, J. 1987, A&A, 184, 1

Brandt, W. N., Lawrence, C. R., Readhead, A. C. S., Pakianathan, J. N., & Fiola, T. M. 1994, ApJ, 424, 1

Bennett, C. L., Larson, D., Weiland, J. L., et al. 2013, ApJS, 208, 20

Casey, C. M., Narayanan, D., & Cooray, A. 2014, Physics Reports, 541, 45

Chapman, S. C., Blain, A. W., Ivison, R. J., & Smail, I. R. 2003, Nature, 422, 695

Chapman, S. C., Blain, A. W., Smail, I., & Ivison, R. J. 2005, ApJ, 622, 772

Condon, J. J. 1992, AR,A&A, 30, 575

Cornwell, T. and Fomalont, E.B., 1989. Self-calibration. In Synthesis Imaging in Radio Astronomy (Vol. 6, p. 185).

Cornwell, T. J. 1988, A&A, 202, 316

Cornwell, T. J. 2008, IEEE Journal of Selected Topics in Signal Processing, 2, 793

Högbom, J. A. 1974, A&As, 15, 417

Cornwell, T. J., & Evans, K. F. 1985, A&A, 143, 77

Sault, R. J. 1990,ApJL 354, L61

Helou, G., Khan, I. R., Malek, L., & Boehmer, L. 1988, ApJS, 68, 151

Coppin, K., Halpern, M., Scott, D., et al. 2008, MNRAS, 384, 1597

Das, S., Sherwin, B. D., Aguirre, P., et al. 2011, Physical Review Letters, 107, 021301

Das, S., Marriage, T. A., Ade, P. A. R., et al. 2011, ApJ, 729, 62

Das, S., Louis, T., Nolta, M. R., et al. 2014, JCAP, 4, 014

Davies, R. D., Watson, R. A., & Gutierrez, C. M. 1996, MNRAS, 278, 925

Draine, B. T. 2003, ARA&A, 41, 241

Draine, B. T., & Lazarian, A. 1998, ApJ, 494, L19

de Zotti, G., Massardi, M., Negrello, M., & Wall, J. 2010, A&Ar, 18, 1

De Zotti, G., & Toffolatti, L. 1998, arXiv:astro-ph/9812069

González-Nuevo, J., Toffolatti, L., & Argüeso, F. 2005, ApJ, 621, 1

Hajian, A., Viero, M. P., Addison, G., et al. 2012, ApJ, 744, 40

Hodge, J. A., Becker, R. H., White, R. L., Richards, G. T., & Zeimann, G. R. 2011, AJ, 142, 3

Becker, R. H., White, R. L., & Helfand, D. J. 1995, ApJ, 450, 559

Condon, J. J., Cotton, W. D., Greisen, E. W., et al. 1998, AJ, 115, 1693

Alpher, V. S. 2014, arXiv:1411.0172

De Zotti, G., Castex, G., González-Nuevo, J., et al. 2015, JCAP, 6, 018

Lagache, G., Bavouzet, N., Fernandez-Conde, N., et al. 2007, ApJL, 665, L89

Dickinson, C., Davies, R. D., & Davis, R. J. 2003, MNRAS, 341, 369

Dole, H., Lagache, G., Puget, J.-L., et al. 2006, A&A, 451, 417

Dünner, R., Hasselfield, M., Marriage, T. A., et al. 2013, ApJ, 762, 10

Dunkley, J., Hlozek, R., Sievers, J., et al. 2011, ApJ, 739, 52

Dunkley, J., Calabrese, E., Sievers, J., et al. 2013, JCAP, 7, 025

Devlin, M. J., Ade, P. A. R., Aretxaga, I., et al. 2009, Nature, 458, 737

Fitt, A. J., Alexander, P., & Cox, M. J. 1988, MNRAS, 233, 907

Finkbeiner, D. P., Davis, M., & Schlegel, D. J. 1999, ApJ, 524, 867

Finkbeiner, D. P. 2003, ApJS, 146, 407

Fomalont, E. B., Perley, R. A., 1999, 'Calibration and editing', In: Synthesis Imaging in Radio Astronomy II, Vol. 180, p. 79.

Fixsen, D. J., Cheng, E. S., Gales, J. M., et al. 1996, ApJ, 473, 576

Carilli, C. L., & Yun, M. S. 2000, ApJ, 530, 618

Thacker, C., Cooray, A., Smidt, J., et al. 2013, ApJ, 768, 58

Amblard, A., Cooray, A., Serra, P., et al. 2011, Nature, 470, 510

Fixsen, D. J., Dwek, E., Mather, J. C., Bennett, C. L., & Shafer, R. A. 1998, ApJ, 508, 123

Fowler, J. W., Niemack, M. D., Dicker, S. R., et al. 2007, Applied Optics, 46, 3444

Fowler, J. W., Acquaviva, V., Ade, P. A. R., et al. 2010, ApJ, 722, 1148

Yun, M. S., Reddy, N. A., & Condon, J. J. 2001, ApJ, 554, 803

Miller, N. A., & Owen, F. N. 2001, AJ, 121, 1903

Garn, T., & Alexander, P. 2008, MNRAS, 391, 1000

George, E. M., Reichardt, C. L., Aird, K. A., et al. 2015, ApJ, 799, 177

Taylor, G. B., Carilli, C. L., & Perley, R. A. 1999, Synthesis Imaging in Radio Astronomy II, 180

Thompson, A. R., Moran, J. M., & Swenson, G. W., Jr. 2001, "Interferometry and synthesis in radio astronomy by A. Richard Thompson, James M. Moran, and George W. Swenson, Jr. 2nd ed. New York : Wiley, c2001.xxiii, 692 p. : ill. ; 25 cm. "A Wiley-Interscience publication." Includes bibliographical references and indexes. ISBN : 0471254924"

Haslam, C. G. T., Salter, C. J., & Stoffel, H. 1981, Origin of Cosmic Rays, 94, 217

Helou, G., Soifer, B. T., & Rowan-Robinson, M. 1985, ApJL 298, L7

Bondi, M., Ciliegi, P., Schinnerer, E., et al. 2008, ApJ, 681, 1129-1135

Sanders, D. B., & Mirabel, I. F. 1996, A&A, 34, 749

Leitch, E. M., Readhead, A. C. S., Pearson, T. J., & Myers, S. T. 1997, ApJL 486, L23

Planck Collaboration, Ade, P. A. R., Aghanim, N., et al. 2015, arXiv:1506.06660

Planck Collaboration, Adam, R., Ade, P. A. R., et al. 2015, arXiv:1502.01582

Planck Collaboration, Ade, P. A. R., Aghanim, N., et al. 2014, A&A, 571, A16

Hinshaw, G., Spergel, D. N., Verde, L., et al. 2003, ApJS, 148, 135

Hughes, D. H., Serjeant, S., Dunlop, J., et al. 1998, Nature, 394, 241

Houck, J. R., Schneider, D. P., Danielson, G. E., et al. 1985, ApJL 290, L5

Holland, W. S., Robson, E. I., Gear, W. K., et al. 1999, MNRAS, 303, 659

Holland, W. S., Bintley, D., Chapin, E. L., et al. 2013, MNRAS, 430, 2513

Ibar, E., Ivison, R. J., Biggs, A. D., et al. 2009, MNRAS, 397, 281

Ivison, R. J., Magnelli, B., Ibar, E., et al. 2010, A&A, 518, L31

Keisler, R., Reichardt, C. L., Aird, K. A., et al. 2011, ApJ, 743, 28

Komatsu, E., Smith, K. M., Dunkley, J., et al. 2011, ApJS, 192, 18

Lagache, G., Puget, J.-L., & Dole, H. 2005, A&A, 43, 727

Larson, D., Dunkley, J., Hinshaw, G., et al. 2011, ApJS, 192, 16

Lasenby, A. N. 1997, Microwave Background Anisotropies, 453

Birkinshaw, M. 1999, Physics Reports, 310, 97

Magnelli, B., Lutz, D., Santini, P., et al. 2012, A&A, 539, A155

Ma, B., Cooray, A., Calanog, J. A., et al. 2015, ApJ, 814, 17

Massardi, M., Bonaldi, A., Negrello, M., et al. 2010, MNRAS, 404, 532

Marsden, D., Gralla, M., Marriage, T. A., et al. 2014, MNRAS, 439, 1556

Marriage, T. A., Baptiste Juin, J., Lin, Y.-T., et al. 2011, ApJ, 731, 100

Magnelli, B., Lutz, D., Berta, S., et al. 2010, A&A, 518, L28

Menanteau, F., Sifón, C., Barrientos, L. F., et al. 2013, ApJ, 765, 67

Mitchell, K. J., & Condon, J. J. 1985, AJ, 90, 1957

Murphy, T. W., Jr., Armus, L., Matthews, K., et al. 1996, AJ, 111, 1025

Neugebauer, G., Habing, H. J., van Duinen, R., et al. 1984, ApJL 278, L1

Murphy, E. J. 2009, ApJ, 706, 482

Schleicher, D. R. G., Schober, J., Federrath, C., Bovino, S., & Schmidt, W. 2013, New Journal of Physics, 15, 023017

Negrello, M., Hopwood, R., De Zotti, G., et al. 2010, Science, 330, 800

Puget, J.-L., Abergel, A., Bernard, J.-P., et al. 1996, A&A, 308, L5

Penzias, A. A., & Wilson, R. W. 1965, ApJ, 142, 419

Planck Collaboration, Aghanim, N., Arnaud, M., et al. 2015, arXiv:1507.02704

Planck Collaboration, Ade, P. A. R., Aghanim, N., et al. 2015, arXiv:1502.01591

Planck Collaboration, Ade, P. A. R., Aghanim, N., et al. 2011, A&A, 536, A13

Reach, W. T., Dwek, E., Fixsen, D. J., et al. 1995, ApJ, 451, 188

Rybicki, G. B., & Lightman, A. P. 1979, New York, Wiley-Interscience, 1979. 393

Reich, P., & Reich, W. 1986, A&AS, 63, 205

Rieke, G. H., Young, E. T., Engelbracht, C. W., et al. 2004, ApJS, 154, 25

Intema, H. T., van der Tol, S., Cotton, W. D., et al. 2009, A&A, 501, 1185

Silk, J. 1968, ApJ, 151, 459

Sievers, J. L., Hlozek, R. A., Nolta, M. R., et al. 2013, JCAP, 10, 060

Simpson, C., Martínez-Sansigre, A., Rawlings, S., et al. 2006, MNRAS, 372, 741

Smail, I., Ivison, R. J., & Blain, A. W. 1997, ApJL 490, L5

Smail, I., Chapman, S. C., Blain, A. W., & Ivison, R. J. 2004, ApJ, 616, 71

Swetz, D. S., Ade, P. A. R., Amiri, M., et al. 2011, ApJS, 194, 41

Soifer, B. T., Rowan-Robinson, M., Houck, J. R., et al. 1984, ApJL 278, L71

Soifer, B. T., & Neugebauer, G. 1991,AJ, 101, 354

Smoot, G. F., Bennett, C. L., Kogut, A., et al. 1992, ApJL, 396, L1

Su, T., Marriage, T. A., Asboth, V., et al. 2016, MNRAS,

Sunyaev, R. A., & Zeldovich, Y. B. 1970, A&AS, 9, 368

Gold, B., Bennett, C. L., Hill, R. S., et al. 2009, ApJS, 180, 265

Planck Collaboration, Adam, R., Ade, P. A. R., et al. 2015, arXiv:1502.01588

Shirokoff, E., Reichardt, C. L., Shaw, L., et al. 2011, ApJ, 736, 61

Story, K. T., Reichardt, C. L., Hou, Z., et al. 2013, ApJ, 779, 86

Carlstrom, J. E., Ade, P. A. R., Aird, K. A., et al. 2011, PASP, 123, 568

Tegmark, M., de Oliveira-Costa, A., & Hamilton, A. J. 2003, Physical Review D, 68, 123523

Tegmark, M., & Efstathiou, G. 1996, MNRAS, 281, 1297

Tegmark, M., & de Oliveira-Costa, A. 1998, ApJL 500, L83

Toffolatti, L., Argueso Gomez, F., de Zotti, G., et al. 1998, MNRAS, 297, 117

Toffolatti, L., De Zotti, G., Argüeso, F., & Burigana, C. 1999, Microwave Foregrounds, 181, 153

Bignell, R. C., & Perley, R. A. 1986, Synthesis Imaging, 49

van der Kruit, P. C. 1971, A&A, 15, 110

Hall, N. R., Keisler, R., Knox, L., et al. 2010, ApJ, 718, 632

Viero, M. P., Moncelsi, L., Quadri, R. F., et al. 2015, ApJL 809, L22

Vieira, J. D., Crawford, T. M., Switzer, E. R., et al. 2010, ApJ, 719, 763

White, M., Scott, D., & Silk, J. 1994, AR, A&A, 32, 319

Zheng, X. Z., Bell, E. F., Rix, H.-W., et al. 2006, ApJ, 640, 78

$https://www.cv.nrao.edu/course/astr534/Interferometers2.html$

$https://science.nrao.edu/facilities/vla/docs/manuals/opt/otf$

$https://casa.nrao.edu/docs/UserMan/casa_cookbook005.html$